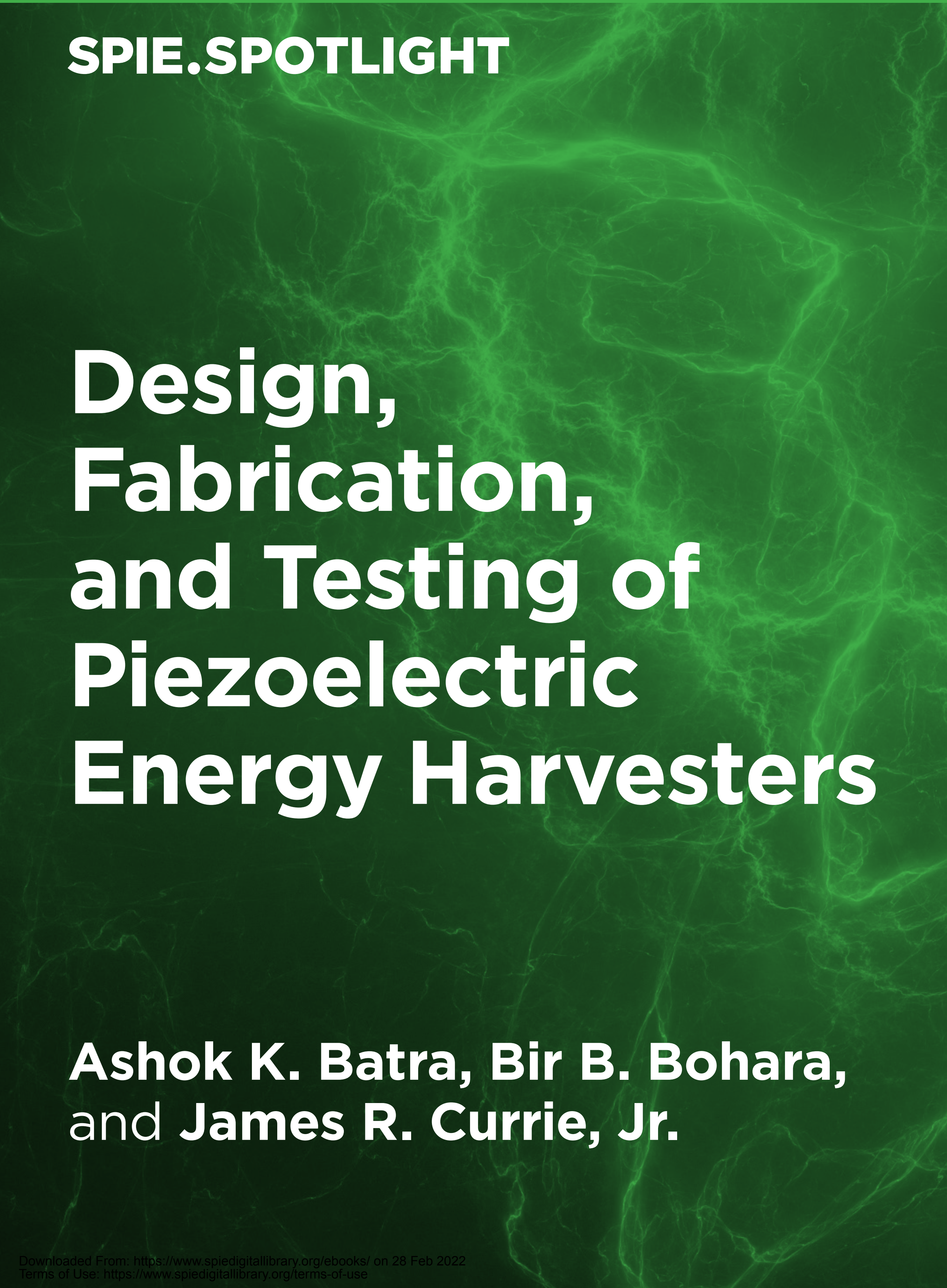

SPIE.SPOTLIGHT

Design, Fabrication, and Testing of Piezoelectric Energy Harvesters

Ashok K. Batra, Bir B. Bohara,
and **James R. Currie, Jr.**

Design, Fabrication, and Testing of Piezoelectric Energy Harvesters

by Ashok K. Batra, Bir B. Bohara,
and James R. Currie, Jr.

doi: http://dx.doi.org/10.1117/3.2504734
PDF ISBN: 9781510622173
epub ISBN: 9781510622180
mobi ISBN: 9781510622197

Published by

SPIE Press
P.O. Box 10
Bellingham, Washington 98227-0010 USA
Phone: +1 360.676.3290
Fax: +1 360.647.1445
Email: Books@spie.org
Web: http://spie.org

Spotlight vol. SL41
Last updated: 6 August 2018

Table of Contents

SPIE Spotlight Series

Welcome to SPIE Spotlight eBooks! This series of tutorials is designed to educate readers about a wide range of topics in optics and photonics. I like to think that these books address subjects that are too broad for journal articles but too concise for textbooks. We hope you enjoy this eBook, and we encourage you to submit your ideas for future Spotlights online.

Robert D. Fiete, *Series Editor*
Harris Corp.

Editorial Board

Preface

Energy harvesting remains a topic of intense interest, and this Spotlight provides a brief timely overview of the energy-harvesting mechanism employed by piezoelectric and pyroelectric candidate materials. Piezoelectric materials provide solid-state conversion between electrical and mechanical energy, can be manufactured at small scale, and can be integrated into microscale devices or even electronic circuits. Several potential materials and device design/configurations along with basic properties are presented. As vibration energy harvesting matures, it is likely that it will be deployed in more hostile environments. The use of pyroelectric harvesting to generate electrical energy from temperature fluctuations is less well studied. Because pyroelectric materials are also piezoelectric, designs that use thermal fluctuations or gradients to generate mechanical motion or an addition of strain to enhance the secondary pyroelectric coefficients are also of interest. Surprisingly, little work has been attempted to combine piezoelectric- and pyroelectric-based harvesting mechanisms. Keeping in view their importance for potential energy harvesters, it is warranted to describe in detail all of the relevant parameters and the available respective measurement techniques. This Spotlight describes all parameters required for piezoelectric and pyroelectric energy harvesters along with measurement techniques used by the authors. Finally, an ambient energy-harvester testing station, developed to investigate the performance of a cantilever-based energy harvester setup in the authors' Clean Energy Laboratory, is described along with the implementation of LabVIEW software to control instruments and acquire data from a piezoelectric energy-harvesting test station. All of the experiments are performed on an isolated optical bench to avoid interference from mechanical noise that may exist in the surrounding environment. The system provides an integrated approach to characterize key performance indicators for energy-harvesting materials and devices.

This Spotlight provides step-by-step instructions to help readers set up their laboratory in order to characterize and analyze the performance of energy harvesters. The state-of-the-art instruments presented herein intended as examples, and alternative products are commercially available.

1 Introduction

Recent developments in ultra-low-power devices, such as wireless sensor nodes, active radio-frequency identification, and nanotransducers, lead to increased demands for ambient energy harvesters to supply self-powered systems. The conversion of low-grade ambient environmental energy, such as mechanical vibration or heat, into usable electrical energy is known as “power harvesting,” “energy harvesting,” or “energy scavenging.” Sensor nodes are widely utilized in remote locations and in applications such as security networks, structure health monitoring, and military systems.[1,2] These active sensors require a self-contained power supply, which, in most cases, is a conventional battery pack. The task of replacing the battery is not practical and is cumbersome for remote locations (glaciers/mountains) or inaccessible locations, including “limited access” or “no-access” structures and toxic environments such as implanted medical devices. The need to replace batteries can also be time consuming and complex to manage, particularly for systems where a large number of wireless sensors are to be deployed. Indeed, in such applications, ambient energy-harvesting solutions have clear advantages. The recent development of ultra-low-power microelectronic devices and sensors has led researchers to the design of passive self-powering devices using ambient energy-harvesting techniques. Mechanical vibration energy generated by machines and the motion of biological systems is one form of wasted energy that could be harvested. Furthermore, this wasted energy can be used to either improve the efficiency of technologies such as computing costs, which could be significantly reduced if wasted “heat” were harvested and used to help power the computer, or enable modern technologies and other devices. Fortunately, most piezoelectric materials are also pyroelectric materials. Thus, we can convert waste energy, both mechanical and heat, using piezoelectric and pyroelectric effects, respectively.[2] The most popular vibration energy-harvesting technique captures power from the electrostatic,[3–6] electromagnetic,[7–12] piezoelectric,[13–16] and magnetostrictive[17–20] vibration energy harvesters (VEHs). The most recent VEH devices are based on a cantilever beam structure, which generates continuous or intermittent resonance frequency tuning. A typical piezoelectric cantilever beam (PCB) can produce maximum power when its resonance frequency matches the frequency of the vibration source.[1] In a number of cases, the vibrations to be harvested consist of a range of frequencies, and researchers have proven that the resonance frequency of a PCB can be modified accordingly by using a variety of different approaches, such as changing the geometrical PCB structure,[21,22] adding a dynamic magnifier,[23–26] using energy-harvesting cantilever arrays,[27–29] and using external magnetic forces.[30,31–36] There are currently a number of researchers who have attempted to capture electric power from passive tuning by magnetic coupling with a PCB.[30,32–36] For example, by applying a magnetic force that acts above the PCB, it is possible to decrease the spring constant and the resonance frequency of the PCB,[30,31] whereas applying an attractive magnetic force along the axis of the PCB applies axial tension and increases the resonance frequency.[37–39] Primarily, the use of ambient energy-harvesting technologies will have a huge impact on socioeconomics and create ample opportunities for new jobs.

Within this context, this Spotlight provides sufficient details regarding experimental work dedicated to the design, fabrication, and testing of piezoelectric energy harvesters (PEHs) based on a system capable of generating energy with both piezoelectric and pyroelectric effects. The aim is to provide an overview of the energy-harvesting technologies associated with the family of “piezoelectric” materials along with the sub-classes of “pyroelectrics.” These materials are very attractive for a number of energy-harvesting applications, including the potential to convert mechanical vibrations directly into electrical energy using the piezoelectric effect and the conversion of thermal fluctuations into electrical energy through the use of the pyroelectric effect.[40]

All ferroelectrics are both pyroelectric and piezoelectric, and all pyroelectrics are piezoelectrics. Because these properties are, in many cases, present in the same material, it produces an interesting characteristic of a material in that can harvest energy from multiple sources, including vibration, thermal fluctuations, and others. The candidate materials are given in Table 1.

2 Ambient Energy Harvesting Using Piezoelectric and Pyroelectric Effects

2.1 Piezoelectric energy harvesting based on the direct piezoelectric effect

In a typical vibrational energy-harvesting system, mechanical energy, such as the applied external force or acceleration, is converted into mechanical energy in the host harvesting structure. Electrical energy is then produced by the piezoelectric material that converts strain into an electric charge, which is finally transferred to a storage medium for later use. Thus, there are three basic processes in vibration harvesting: (i) conversion of the input vibrational energy into mechanical energy (mechanical strain), (ii) electromechanical conversion (piezoelectric transduction), and (iii) electrical energy transfer. PEHs offer a number of advantages compared to other transduction mechanisms, including high-energy conversion, high-energy density, high-output voltage but low-current level, and high-output impedance, including ease of integration with other systems.[38] The performance of a PEH device based on a PCB is evaluated by the determination of the resonance frequency of the structure at a variety of electrical and mechanical loads. Thus, measuring input and output voltages, acceleration, displacement, and the frequency of vibration are desired practical parameters to fully characterize a PEH.

Table 1 Dielectric, piezoelectric, mechanical, and pyroelectric properties of some candidate materials for PEHs and pyroelectric energy harvesters.[41]

Materials	**AlN**	**ZnO**	**$BaTiO_3$**	**PZT-4**	**PZT-5H**	**PMN–PT**	**PVDF**
Piezoelectric	Yes	Yes	Yes	Yes	Yes	Yes	Yes
Pyroelectric	Yes	Yes	Yes	Yes	Yes	Yes	Yes
Ferroelectric	No	No	Yes	Yes	Yes	Yes	Yes
Const. strain rel. ($\varepsilon^{s}{}_{33}$)	10.0	8.84	910	635	1470	680	5 to 13
Const. stress rel. ($\varepsilon^{T}{}_{33}$)	11.9	11.0	1200	1300	3400	8200	7.6
d_{33} pC N^{-1}	5	12.4	149	289	593	2820	–33
d_{31} pC N^{-1}	–2	–5.0	–58	–123	–274	–1330	21
d_{15} pC N^{-1}	3.6	–8.3	242	495	741	146	–27
Mechanical quality (Q_m)	2490	1770	400	500	65	43 to 2050	3 to 10
E-M coupling (k_{33})	–0.23	0.48	0.49	0.7	0.75	0.94	0.19
Pyro. coefficient P (μC m^{-2} K^{-1})	6 to 8	9.5	200	260 to 533	260 to 533	1790	33
$s^{E}{}_{11}$ (pPa^{-1})	2.854	7.86	8.6	12.3	16.4	69.0	365
$s^{E}{}_{33}$ (pPa^{-1})	2.824	6.94	9.1	15.5	20.8	119.6	472

The materials given in Table 1 are piezoelectric. Crystals that procure a charge when compressed in any way are called piezoelectric. This behavior provides a useful transducer effect between electrical and mechanical oscillations. The nature of the piezoelectric effect is related to the existence of electric dipole moments in solids. The change of polarization is of importance for the piezoelectric effect, in particular when applying mechanical stress, produced by either a reconfiguration of the dipole-inducing surroundings or by reorientation of molecular dipole moments under the effect of the external stress. Figure 1 illustrates the mechanisms of direct piezoelectricity.

2.2 Piezoelectric effect for energy harvesting

The greatest use of energy captured from the environment involves converting it into electrical energy, which requires an energy harvester or energy scavenger. A harvester is an energy-harvesting device designed to convert mechanical energy into electricity, depending on the characteristics of the environmental motions. A system like this usually has a resonant frequency that can be designed to match the characteristic frequency of the environmental motions. Detailed analysis of the mechanisms of mechanical energy harvesting can be found elsewhere.[1,38]

3 Design and Fabrication of Energy Harvesters

Piezoelectric materials are non-centrosymmetric crystalline materials that have dipole moments. When an external strain is applied, they generate an output voltage. This effect in piezoelectric materials is known as a direct piezoelectric effect, which is utilized in PEHs. On the other hand, the application of an electric field on the surface of piezoelectric materials produces a strain on the materials, i.e., an indirect piezoelectric effect. Depending on their structures, piezoelectric materials can be classified into four groups: single crystals (SCs), polymers, composites,

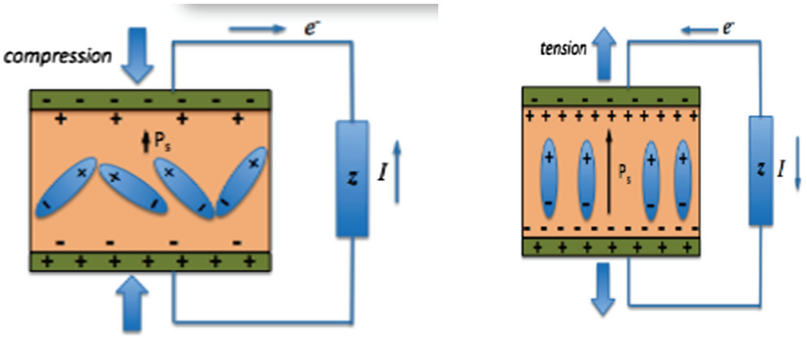

Figure 1 Mechanisms of piezoelectricity.

and ceramics. Some typical examples of the most-used piezoelectric materials include the ceramic lead zirconate titanate (PZT), the SC lead magnesium niobate-lead titanate (PMN-PT), and the polymer polyvinylidene fluoride (PVDF). All of these are sub-groups of piezoelectric materials called "ferroelectrics." These materials possess a permanent dipole below the Curie temperature, which makes them piezoelectric. The ferroelectric SCs, ceramics, composites, and polymers have their own advantages and limitations. PVDFs have high flexibility and strength, which makes them suitable for applications in large bending or curved mounting surfaces but have a relatively low charge coefficient. Although ferroelectric SCs, ceramics, and composites have superior piezoelectric characteristics to polymers, they have poor flexibility and strength.

The various kinds of piezoelectric transducers, such as monomorphs, bimorphs, membranes, or stacks, can be utilized for energy scavenging from ambient sources. Because a single configuration is not suitable for all applications, energy harvesters, in general, are designed for a specific purpose with a certain frequency range. As the piezoelectric power output is maximized at resonance frequency, the efficiency and power density of piezoelectric vibration energy are strongly frequency dependent. The typical vibration frequency of human and animal motions ranges from 1 to 30 Hz, whereas machinery equipment has a frequency of 100 Hz or higher. Piezoelectric ceramics are normally used for higher vibration frequencies (100 Hz or higher) because of the suitability of the fabricated elements with higher resonance frequencies. But the fabrication of lower-frequency VEHs is complicated because of the limits of the dimensional and weight constraints. Because of its high flexibility and low natural frequency, the PCB is the most popular structure in energy harvesting. A tip mass at the free end reduces the natural frequency and enhances deflection. Based on the fact that the power-harvesting performance of a piezoelectric harvesting device is limited to the resonance excitation, new technologies have been exploited.[42–52]

3.1 Cantilevered energy harvesters and types of cantilever beams

Most of the recent PEH studies have focused on generating vibrations from a free source of vibration, such as a cantilever beam. The reasons and advantages for using cantilever beams are given in this section. Cantilevered PEHs have attracted the most attention from researchers for several reasons. First, most of the ambient vibrations occur at a low frequency (below 200 Hz), and a cantilever beam has the lowest stiffness for a given size; thus, it is easier to design a low-frequency PEH by using a cantilever beam. Second, the power output is proportional to the average strain in the PEH, and the cantilever beam generates the highest average strain for a given mechanical load. In addition, the cantilever beam is easy to fabricate and install. When using a cantilever beam, it is fixed at one end and free at the other (Fig. 2). A cantilever-beam piezoelectric generator can be one of three types: unimorph, bimorph series, or parallel configuration.[1]

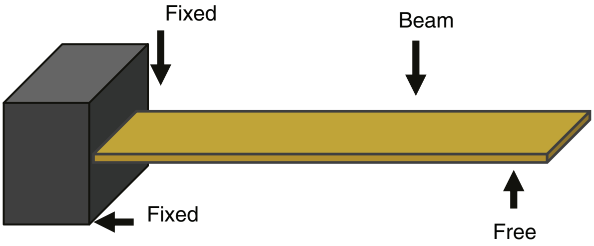

Figure 2 Cantilever beam.

3.1.1 Unimorph cantilever

When the beam has only one piezoelectric layer (PL) attached to the substrate or non-piezoelectric layer (NPL), as shown in Fig. 3, the device is known as a piezoelectric unimorph cantilever.

3.1.2 Bimorph cantilever

A piezoelectric bimorph cantilever consists of two PLs sandwiching a NPL, as shown in Fig. 4. The two PLs usually consist of the same material with the same dimensions. The purpose of a NPL is to provide mechanical support and electrical connection. The two PLs can be connected in series [Fig. 4(a)] or parallel [Fig. 4(b)] to generate a high voltage or current, respectively.

3.1.3 Multimorph cantilever

A multimorph cantilever has more than two PLs. It is not as popular as the unimorph and bimorph cantilevers due to its complexity of fabrication. One, two, and five thin-film PLs of the same total thickness can be used, as shown in Fig. 5, in a multimorph cantilever.[1] The voltage output is inversely proportional to the number of PLs.

The cantilever model can be used in two different modes: 33-mode and 31-mode. The former (compressive or longitudinal mode) means that the voltage is obtained in the three directions parallel to the direction of the applied force.

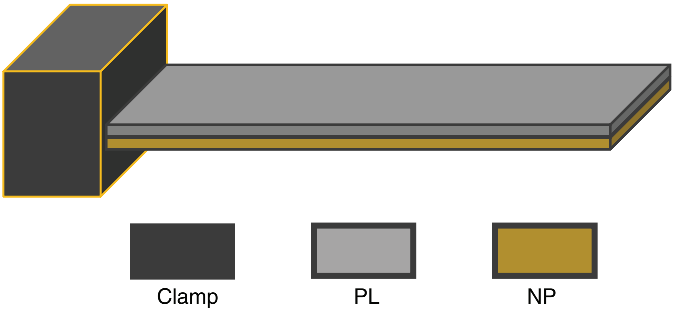

Figure 3 Piezoelectric unimorph cantilever.

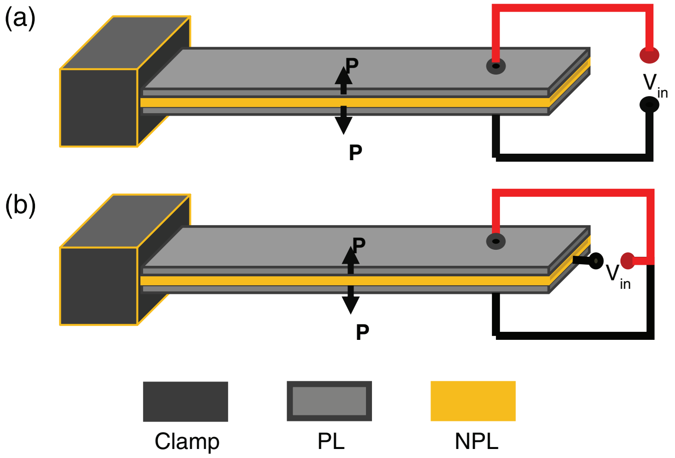

Figure 4 Piezoelectric bimorph cantilevers in (a) serial and (b) parallel connections. Arrows indicate the poling direction.

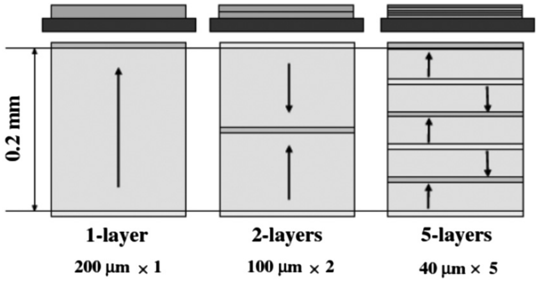

Figure 5 Multilayer PEH.[1]

The latter (transverse mode) means that the voltage is obtained in the one direction perpendicular to the direction of the applied force. The 31-mode is most useful for harvesting applications because an immense proof mass would be needed for the 33-configuration.

3.2 Modeling cantilever beams

An investigation of the output parameters of a cantilevered energy harvester requires a complete physical and theoretical description of the electromechanical interactions of the system. This combined mechanical system represents a cantilever beam, and an electrical source represents a piezoelectric material. Mechanical vibrations produce an oscillating motion of the piezoelectric material. The resulting strain on the PL generates an alternating current (AC) voltage signal along the electrode layer. Mechanical vibration in a cantilever beam follows the linear theory of elasticity and can be simplified using the Euler–Bernoulli beam theory. However, this theory is a simple theoretical method to calculate the load carrying and deflection of thin beams; it is also a special case of the Timoshenko beam theory, which deals with thick beams and accounts for shear deformation and the rotational inertia effect. In recent centuries, additional analyses have been developed, such as plate theory and finite-element analysis.

3.3 Design optimization technique of polyvinylidene fluoride-based piezoelectric energy harvesters

It is always desirable to optimize the performance of any device to obtain the maximum output through the interdependent respective properties and parameters. In the case of PEHs, the properties of the piezoelectric materials are important and powerful factors that can be used to improve their output capability. However, in PEHs, the potential of the material is less likely to be fully exploited without an optimized configuration. Song et al.[53] recently proposed an optimization strategy for a PVDF-based cantilever-type PEH to achieve the highest output power density with the given frequency and acceleration of the vibration source. The authors reported that the maximum power output density only depends on the maximum allowable stress of the beam and the working frequency of the device. These two parameters can be obtained by adjusting the geometry of the PLs. A fabricated device with a volume of 13.1 mm^3 showed an output power of 112.8 μW, which is comparable to the best-performing piezoelectric-based energy harvesters with a similar volume.

3.3.1 Configuration of a polyvinylidene fluoride-based bimorph piezoelectric energy harvester

Figure 6 illustrates the basic structure of a PVDF-based PEH device.[53] The bimorph cantilever beam is completely made of PVDF film, with the steel load mass adhered to the free end of the beam that is clamped by the fixed end. The PVDF films are each 50 μm thick, with a thin Ag electrode on the surface, and are bonded in the same polling and stretching directions. The adhesive layers between the PVDF films and the two pieces of load mass are attached to the end of the PVDF beam with an epoxy whose thickness can be ignored. The two layers of the PVDF are connected in parallel in the circuit with a resistance as an output load.

3.3.2 Analytical modeling of a bimorph piezoelectric energy harvester

Song et al.[53] suggested two approximations due to the low electromechanical coupling coefficients of PVDF ($k_{31} \ll 1$) in the following analysis: (i) the optimum

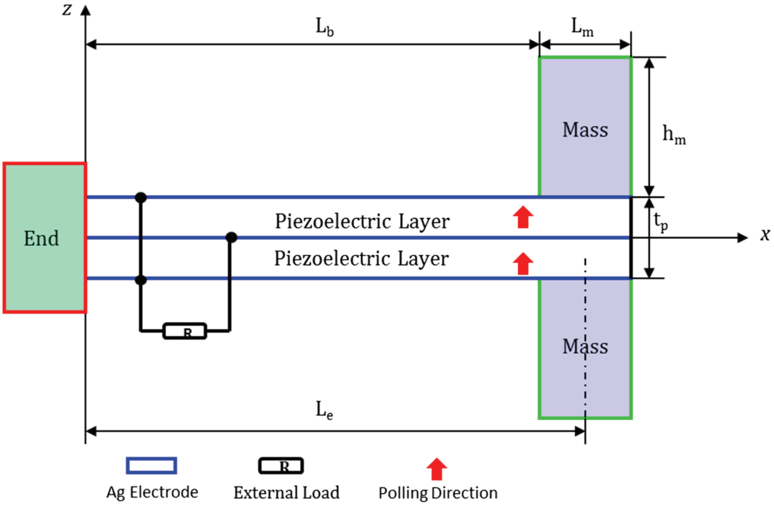

Figure 6 Configuration of a PVDF-based PEH device.

working frequency of the harvester equals the natural frequency of the beam, and (ii) the indirect piezoelectric effect is neglected.

The optimum working frequency of the device with an external load lies between the open-circuit frequency (f_{open}) and the short-circuit frequency (f_{short}). Furthermore, the natural frequencies of a piezoelectric beam under open- and short-circuit conditions are correlated:[23]

$$f_{\text{short}} = f_{\text{open}}\sqrt{1 - k_{31}^2}. \tag{1}$$

As the k_{31} of a PVDF is only about 0.12,[2,21] the difference between f_{open} and f_{short} is commonly within 1%. The electromechanical coupling coefficient of the device is even lower than that of the material.

Typically, the cantilever under vibration excitation can be approximately treated as a spring with damping and a point mass, as illustrated in Fig. 7(a).

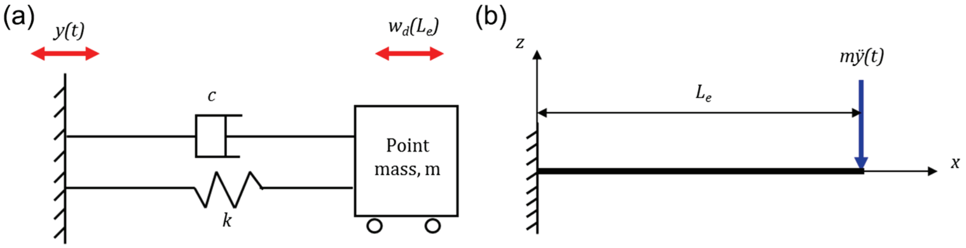

Figure 7 (a) The damping and (b) the excitation model.

When $L_b \gg L_m$ and $m_m \gg m_b$ (m_m and m_b represent the weight of the end mass and the cantilever beam, respectively), an effective length of the cantilever L_e, which is equivalent to $L_b + L_m/2$, and an effective mass m, which is approximately equal to m_m, can be used to depict the system as a cantilever with a point end mass. The equivalent stiffness of the beam is then written as

$$K = \frac{3EI}{L_e^3}, \tag{2}$$

where E is the elastic modulus of the beam material, and I is the moment of inertia of the beam. Accordingly, ω_n can be derived as

$$\omega_2^n = \frac{EW_b t_p^3}{4mL_e^3}. \tag{3}$$

Then the movement of the point mass, in which the reverse piezoelectric effect is not involved, can be expressed as

$$m\frac{d^2 w_d L_e}{dt^2} + c\frac{dw_d(L_e)}{dt} + kw_d(L_e) = -m\frac{d^2 y}{dt^2}, \tag{4}$$

where $c = 2\xi m\omega_n$, and ξ represents the damping factor; the motion of the vibration source is treated as $y(t) = A\cos(\omega t)$, where ω stands for the angular frequency; and $w_d(L_e)$ represents the displacement of the mass. For a sinusoidal vibration source, $w_d(L_e)$ can be expressed as $w_d(L_e) = w_0\cos(\omega t + \theta)$. Substituting the expression of $w_d(L_e)$ in Eq. (4), W_0 can be solved as $\omega = \omega_n$:

$$W_0 = \frac{m\omega_n^2 A}{2k\xi}. \tag{5}$$

In order to determine the displacement of the neutral plane of the beam at any point $w_d(x)$ along its length, the excitation acting on the cantilever beam through the fixed end can be equivalent to a point force [my, $m\ddot{y}(t)$] applied at its free end, which is illustrated in Fig. 7(b). Then $w_d(x)$ can be expressed as $w_d(x) = w_0\phi(x)\cos(\omega t + \theta)$, where $\phi(x)$ is the normalized shape function representing the amplitude ratio of the points at x and L_e:

$$\phi(x) = c\frac{(L_e - x)^3}{2L_e^3} + \frac{(L_e - x)}{2L_e} + 1. \tag{6}$$

In a linear elastic beam, the stress in the x direction in a PVDF beam can be expressed as

$$\sigma_x(x,z) = E_z\frac{d^2 w_d x}{dx^2}, \tag{7}$$

where z represents the distance to the neutral layer of the beam. With Eqs. (6) and (7) for the expression of $w_d(x)$, the maximum stress can be solved at $\sigma_{\max} = \sigma\ (0,\ 1/2t_p)$. A relation between ω_{res} and $\sigma_{\max}$ can be obtained as in Eq. (8) with the vibration source's acceleration ACC $= A\omega_n^2\omega$:

$$\sigma_{x\max} \cdot \omega_n^2 = \frac{3E}{4\xi} \cdot \frac{t_p}{L_e^2} \mathrm{ACC}. \tag{8}$$

The piezoelectricity of the PVDF dictates that the relation of electric displacement D_3, electric field E_3, and stress σ_x can be expressed as

$$D_3 = d_{31}\sigma_{3x} + \varepsilon_p^\sigma, \tag{9}$$

where d_{31} is the piezoelectric constant in 31-mode, and $\varepsilon_p^\sigma\varepsilon$ is the permittivity of the PLs under the condition of constant stress. D_3 is uniform within each layer of the PVDF as there are no free charges within the PVDF. By integrating Eq. (9) in the z direction from the neutral layer to the top surface of the beam, E_3 can be replaced by the output I_R:

$$\begin{aligned} D_3 &= \frac{\int_0^{\frac{1}{2}t_p} D_3 dz}{\frac{1}{2}t_p} = \frac{d_{31}E\frac{d^2w_d(x)}{dx^2}\int_0^{\frac{1}{2}t_p} z dz + \varepsilon_p^\sigma \int_0^{\frac{1}{2}t_p} E_3 dz}{\frac{1}{2}t_p} \\ &= d_{31}E\frac{t_p}{4}\frac{d^2w_d(x)}{dx^2} - \frac{2\varepsilon_p^\sigma}{t_p} I_R \cdot R, \end{aligned} \tag{10}$$

where R represents the resistive load in the circuit. By integrating Eq. (10) with the total beam surface, the generated charge Q_0 can be expressed as

$$Q_0 = \iint_s D_3 dx dy = \frac{3EW_b d_{31} t_{pW_0}}{4L_e}\cos(\omega t + \theta_1) - c_{\mathrm{equ}} \cdot I_R \cdot R, \tag{11}$$

where C_{equ} represents the capacitance of one PVDF layer. Since $I_R = dQ_0/dt$, differentiating both sides in Eq. (11), and substituting $I_R = I_0$, $\cos(\omega t + \theta_2)$ leads to an equation for I_0. Then the average output power P can be deduced:

$$\begin{aligned} P &= \frac{I_0^2 \cdot R}{2} \\ &= \frac{9E^2W_b^2d_{31}^2t_p^2W_0^2}{64L_e^2} \cdot \frac{R}{1 + (\omega c_{\mathrm{equ}}R)^2} \le \frac{9E^2W_b^2d_{31}^2t_p^2W_0^2}{64L_e^2} \cdot \frac{1}{2\omega c_{\mathrm{equ}}}. \end{aligned} \tag{12}$$

When and only when $R = 1/\omega\, C_{\text{equ}}$, P reaches its maximum value. We call this R the optimum resistance, and the maximum power at resonant frequency can be expressed

$$P_{\max} = \frac{9E^2 d_{31}^2 A^2 m^2 \omega_n^2 t_p^3 W_b}{64L_e^2} = \frac{d_{31}^2 d_{31}^2}{64\varepsilon_p^\sigma}\omega_n \sigma_{\max}^2 (W_b L_e t_p). \tag{13}$$

By adding the expression for $\sigma_{\max}$, as shown in Eq. (8), into Eq. (13), the output power density is obtained:

$$\frac{P}{V_{\max}} = \frac{P_{\max}}{W_b L_e t_p} = \frac{d_{31}^2}{64\varepsilon_p^\sigma}\omega_n \sigma_{\max}^2 \leq \frac{d_{31}^2}{64\varepsilon_p^\sigma}\omega_n \sigma_{\text{yield}}^2, \tag{14}$$

where V stands for the effective volume of the cantilever. It is interesting that the output power density is determined solely by $\sigma_{\max}$ and ω_n. For a given vibration environment, there exists a maximum power density that is determined by the maximum stress allowed in the cantilever. Thus, the maximum output power density of a PVDF-PEH is achieved when $\sigma_{\max}$ reaches σ_{yield} (or σ_{yield} divided by a safety factor for practical use) by adjusting t_p/L_e^2, as shown in Eq. (8). In other words, for each given ω_n, there is an optimal t_p/L_e^2 to maximize the output power density, and m/W_b is determined by Eq. (3) accordingly, which leads to optimized device configurations. Figure 8 presents the dependence of the optimal L_e and t_p on f_{res} for a given ACC = 10 m/s^2 and the given commercially available PVDF film with $\sigma_{\max} = 30$ MPa. Notably, the maximum output power density does not depend on the vibration acceleration amplitude ACC, although the optimal L_e does.

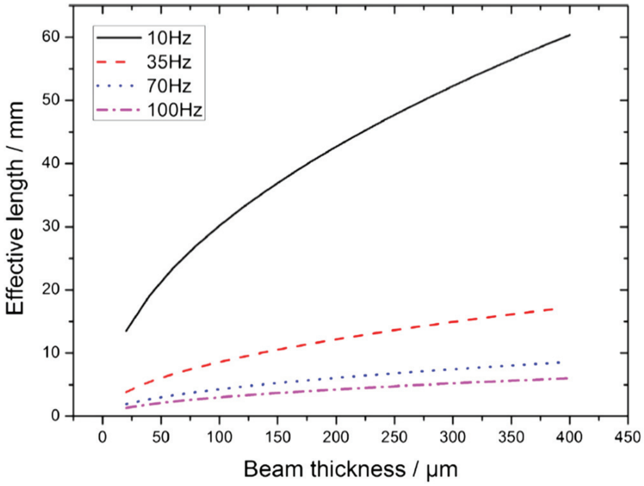

Figure 8 The dependence of optimal L_e and t_p at different resonant frequencies for ACC = 10 m/s^2 and $\sigma_{\max} = 30$ MPa.

3.3.3 Optimized configuration of polyvinylidene fluoride-based piezoelectric energy harvesting

This section describes the determination of an optimized PVDF-based PEH excited by a vibration source working at 35 Hz (a frequency easily found in the surrounding environment) and with an ACC of 0.5 g, whose performance will be verified with finite-element simulation and experimental test.[42] To ensure that the PEH can work sustainably over a long period, $\sigma_{\max}$ should be sufficiently lower than σ_{yield} (~42 MPa[25]); thus, we set $\sigma_{\max} = 30$ MPa for the optimization of the device. The commercially available PVDF sheets used for device fabrication are 50 μm thick, which makes the total thickness of the beam 100 μm. By using the data of a PVDF in Table 2, the optimum t_p/L_e^2 can be worked out using Eq. (8), and L_e is known. The weight of the end mass m and the width of the beam W_b can be determined from Eq. (3) plus the limit (preference) of the area of the device with known ω_n, t_p, and L_e. Note that L_e is determined by a combination of L_b and L_m, and can set them with a certain freedom as long as $L_b \gg L_m$ is satisfied. Kanda et al.[42] set L_m to 2 mm for convenience, and L_b and h_m can be worked out accordingly. R_{opt}, which is needed for the testing of the device, can be calculated from $R_{\text{opt}} = 1/\omega \cdot C_{\text{equ}}$. Once the shape of the device is determined, the final configuration parameters of the designed device are listed in Table 3. The expected output power density can reach 15.4 mW/cm^3 according to Eq. (14), which is on the same level of the best-performing piezoceramic-based PEH devices.[26–29,31]

3.4 Design of a piezoelectric element

A variety of cantilever configurations are available in the literature.[1] The main focus is to enhance their performance along with a wide frequency response. Figure 9 illustrates a thick-film piezo–pyro element.

PVDF is a highly non-reactive thermoplastic fluoropolymer that has a piezoelectric coefficient 10 times larger than any other polymers. It is also a material of high flexibility, high toughness, and can be readily formed into a thin-film profile. Figure 10 shows a commercially available transducer made of PVDF with electrodes.

PZT is an intermetallic inorganic compound with the chemical formula $Pb[Zr_x Ti_{1-x}] O_3$ $(0 \leq x \leq 1)$. A commercially available PZT-based epoxy cantilever and encapsulation are illustrated in Fig. 11.

PMN-PT has a higher electromechanical coupling than conventional piezoceramics that possess exceptional properties and is poised to revolutionize applications from medical ultrasound to adaptive optics and energy harvesting. A SC-based cantilevered harvester is illustrated in Fig. 12.

Nanopaint PZT-composite is a thick film of a composite (special paint + PZT nanopowder), which was fabricated using cost-effective conventional brush-painting on a copper substrate and was later silver electroded, as illustrated in Fig. 13.

Table 2 Material parameters of the PVDF-based PEH.[42]

Piezoelectric constants (pC/N)	d_{31}	23.9	Coupling coefficients	k_{31}	0.14
	d_{33}	–32.5		k_{33}	0.19
Young's modulus (GPa)	E	4.18	Density (kg/m^3)	p_b	1700
Elastic constants (10^{-11} Pa^{-1})	S_{11}	23.9	Relative dielectric	ε_r	13
	S_{12}	–7.18	Constant	Q_m	17.2
	S_{13}	–7.18	Mechanical quality	ξ	0.0291
	S_{44}	62.2	Factor	t_b	50
	S_{66}	62.2	Damping factor in air thickness (μm)	σ_{yield}	50
			Yield strength (MPa)		
Seismic mass material characteristics					
Young's modulus (GPa)	E	200	Poisson's ratio	υ	0.29
			Density (kg/m^3)	p_m	7800

Table 3 Calculated parameters of the configuration.[42]

Dimension of the PVDF film (mm, two layers)	$L_e \times W_b \times t_p$	$6.3 \times 20 \times 0.1$
Dimension of the seismic mass (mm, one block)	$L_m \times W_m \times h_m$	$2 \times 20 \times 3$
Equivalent capacitance (pF)	C_{equ}	672
Optimum resistance (MΩ)	R_{opt}	6.76
Maximum power density (mW/cm^3)	$(P/V)_{\max}$	15.4

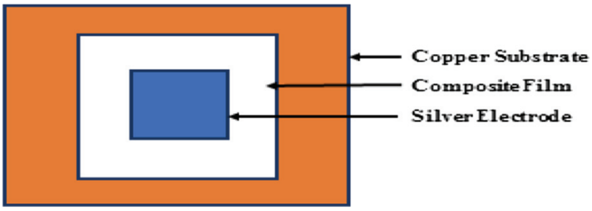

Figure 9 Design of the piezoelectric/pyroelectric element.

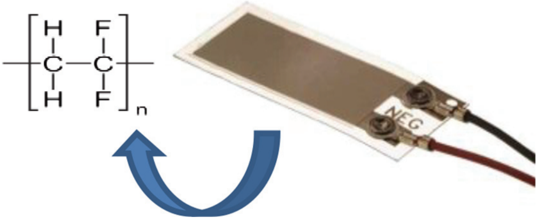

Figure 10 A photograph of a PVDF-based transducer.

Figure 11 A photograph of a PZT cantilever clamped at one end.

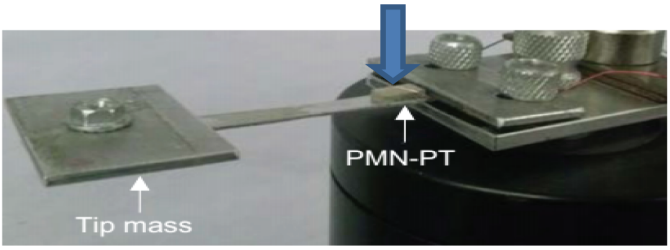

Figure 12 A PMN-PT SC-based cantilever.

Figure 13 Design of the pyroelectric/PEH cantilever.

3.4.1 Fabrication of an energy harvester utilizing a number of technologies

Design of a Cantilevered Energy Harvester by Theoretical Modeling. Selection of Materials Based on Configuration and Fabrication Process

↓

- ▪ Cleaning and washing of substrate to be used as cantilever
- ▪ Coating of bottom electrode if required via sputtering or thermal evaporation

↓

Fabrication of thin film on coated cantilever with one of the following techniques:

- ➢ Sputtering technique
- ➢ Sol-gel technique
- ➢ Laser ablation
- ➢ Chemical-vapor deposition
- ➢ Spin coating

Fabrication of bulk material/thick film/single crystalline/composite-based cantilever with one of the following techniques:

- ➢ Screen printing
- ➢ Doctor blading
- ➢ Brush painting
- ➢ Solution casting
- ➢ Flux technique for crystal growth
- ➢ Ceramic processing

↓

- ❖ Electrode formation onto a coated functional film with thermal evaporation or sputtering, if required
- ❖ Poling with an appropriate method
- ❖ Wire bonding and encapsulation, if needed
- ❖ Testing for determination of performance of the harvester

4 Pyroelectric Energy Harvesting Based on the Direct Pyroelectric Effect

4.1 Pyroelectric-based harvesting

The pyroelectric effect is exhibited by polar materials due to the temperature dependence of their electrical polarization.[54] Pyroelectric materials are of interest due to their high-thermodynamic efficiency, and unlike thermoelectrics they do not require bulky heat sinks to maintain a temperature gradient. One of the technical challenges in pyroelectric harvesting systems is to develop methods to generate temperature oscillations to harvest power. An additional challenge is that the inherent large thermal mass of materials generally restricts pyroelectric harvesters to low-frequency operation compared to vibration harvesters.

The following section presents the capabilities of pyroelectric materials in harvesting energy when subjected to cyclic or linear temperature variations. A pyroelectric material is considered to exhibit no losses with purely linear properties, assuming a limited heat exchange on the outer surface of the pyroelectric element.

4.2 Pyroelectric energy-harvesting figures of merit

For unclamped pyroelectric materials, the expressions for charge, the voltage generated, and energy stored in a pyroelectric material can be derived as follows: the net charge developed due to the temperature change ΔT is given by

$$Q = pA\Delta T. \tag{15}$$

The pyroelectric materials are typically dielectric in nature. The equivalent capacitance C is given by

$$C = \frac{A}{h}\varepsilon_{33}, \tag{16}$$

where ε_{33} is the permittivity in the polarization direction at constant stress. The open-circuit voltage V and electric field E_f developed across the electrodes, from $Q = CV$, can be expressed as follows:[44]

$$V = \frac{p}{\varepsilon_{33}}h\Delta T \tag{17}$$

and

$$E_f = \frac{p\Delta T}{\varepsilon_{33}}. \tag{18}$$

Because the total energy E stored in a capacitance is $1/2CV^2$, this value represents the amount of energy stored in the material at the end of the temperature change and is calculated with Eqs. (17) and (18):

$$E = \frac{1p^2}{2\varepsilon_{33}}Ah(\Delta T)^2. \tag{19}$$

A variety of figures of merit (FoMs) have been derived, such as

$$F_i = \frac{p}{c_E} = \frac{p}{\rho c_p}, \tag{20}$$

for high-current responsivity, where c_E is the volume-specific heat, c_p is the specific heat capacity, and ρ is the density of the pyroelectric chip. For high-voltage responsivity, the FoM F_v is given by

$$F_v = \frac{p}{\rho \varepsilon_{33} c_p}. \tag{21}$$

For energy-harvesting applications, two pyroelectric-based FoMs have recently been proposed. An electrothermal coupling factor has been defined to estimate the effectiveness of thermal harvesting:

$$k^2 = \frac{p^2 T_{\text{hot}}}{\rho \varepsilon_{33} c_p}, \tag{22}$$

where T_{hot} is the maximum working temperature. This FoM has a direct influence on the efficiency and electrical work obtained during cyclic temperature-oscillation cycles. For many materials, the value is low (<1%); some examples are given in Table 4.

An energy-harvesting FoM F_E has also been proposed:

$$F_E = \frac{p^2}{\varepsilon_{33}} \tag{23}$$

and has been widely used for material selection and design.

Bowen et al.[41] proposed and derived an alternative pyroelectric harvesting FoM that includes the influence of the heat capacity from Eq. (23). The relationship between the input enthalpy H and the resulting temperature change ΔT is $H = Ahc_E \Delta T$; substituting this value into Eq. (23) gives a new energy-harvesting FoM:[54]

$$F'_E = \frac{p^2}{\varepsilon_{33} (c_E)^2}. \tag{24}$$

A higher value of F'_E implies that a larger amount of energy is converted by the materials for a given enthalpy input. The relevant properties and calculated FoMs are described in Table 4 for the comparison and selection of materials for energy harvesting.

Table 4 Pyroelectric energy-harvesting FoMs for candidate materials.

Parameter	Units	PMN-0.25PT (SC)	PZT (ceramic)	PVDF (film)	ZnO (SC)	LiTaO$_3$ (SC)
p	μC/m^2 K	1790	533	33	9.4	230
$\varepsilon_{33}/\varepsilon_0$	—	961	1116	9	11	47
c_E	MJ/m^3/K	2.5	2.5	1.8	2.3	3.2
k^2	%$T_h = 298$ K	4.5	0.34	0.23	0.01	1.18
F_E	J/m^3/K^2	376.7	28.8	13.6	0.91	12.4
F'_E	m^3/J	60.3	4.6	4.2	0.17	12.4

Table 4 shows that the FoM F_E (as well as PZT and $LiTaO_3$) for PMN-PT is particularly high due to a high pyroelectric coefficient p. The F_E' for PMN-PT is also high, and that material remains of interest in terms of high performance in energy harvesting; however, the low volume-specific heat of PVDF leads to a high F_E'. PVDF-based materials are flexible, low cost, damage tolerant, easily manufactured in thin and large area sections, and have a high breakdown strength. PVDF composite systems may be of interest for achieving a high F_E' value by maintaining a high p but reducing both the permittivity and volume-specific heat. Based on these parameters, newly designed composites can be found for a high F_E'.

5 Hybrid Piezoelectric and Pyroelectric Energy Harvester

PEHs, in which time-dependent temperature fluctuations are converted into electrical energy by the pyroelectric effect, are less widely explored. To enhance or supplement the performance of the energy-harvesting device, it is of interest to develop a technology to simultaneously or individually harvest both the mechanical and thermal energies using an integrated device. Fortunately, there are ferroelectric materials, such as PZT and PMN-PT that, when polarized, exhibit piezoelectric and pyroelectric properties.[40] The mechanism is presented in Fig. 14.

The pyroelectric voltage output response of a harvester was tested with respect to temperature gradient under different frequencies of a vibration PEH. Figure 15 shows the variation of the output voltage versus temperature for a PMN-PT SC at frequency values of 8, 11, 30, 40, and 49 Hz. Figure 15 indicates that the VEH showed an increase in output voltage with temperature up to 180% of its original value under a temperature difference of 1.7°C. However, the maximum increase in voltage was obtained at a resonance frequency of 49 Hz and a optimum resistance of 2 MΩ under a base excitation of 1 g. The changes of piezo/pyro voltage at different temperatures, required times, and percentage increases in voltage are summarized in Table 5.

Finally, the performance of a multisource energy harvester to simultaneously harvest thermal and mechanical energies by the use of a SC PMN-PT patch was investigated by Alomari et al.[40] It was demonstrated by the authors that there is an increase in output voltage with the temperature gradient, and the maximum AC output voltage at a resonance frequency value of 49 Hz was increased from 1.045 to 2.935 V under a temperature gradient of 1.7°C.

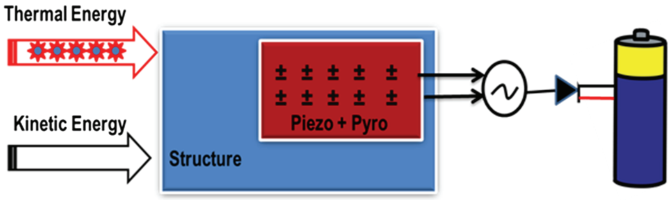

Figure 14 Concept and principle of a piezoelectric and pyroelectric mechanism.

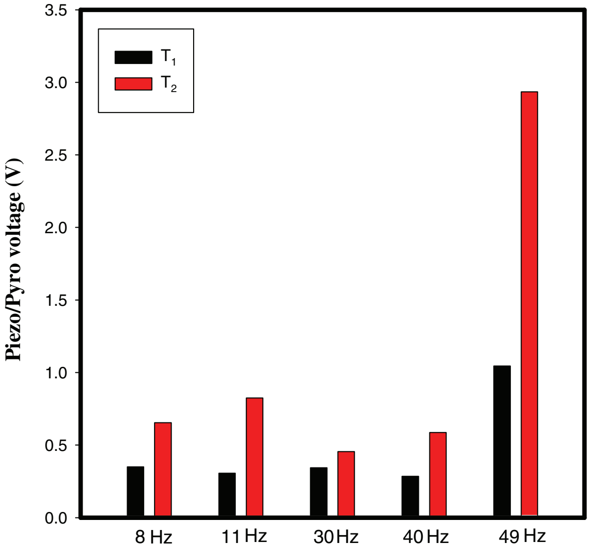

Figure 15 Variation of the output voltage at initial and final temperatures for a PMN-PT SC at different frequency values.

Table 5 Piezo/pyro voltage, temperature difference, required time, and percentage increase in voltage (%) for a PMN-PT SC at different frequency values.

Frequency (Hz)	V_1 (V)	V (V)	ΔT (°C)	Required time (s)	Percentage increase in voltage (%)
8	0.351	0.655	1.8	19.50	86
11	0.306	0.824	1.6	26.24	169
30	0.344	0.456	0.4	15.40	32
40	0.285	0.587	1	29.20	105
49	1.045	2.935	1.7	30.11	180

6 Characterization of the Piezoelectric Element and Testing of Piezoelectric Energy Harvesters

The electrical, mechanical, and electromechanical parameters of piezoelement characterization along with the system for testing of a PEH are described in this section. The aforementioned parameters are utilized for modeling and simulation of PEHs. A description of all of the state-of-the-art instrumentation, including specifications and manufacturer, is also included to set up an energy-harvester testing laboratory.

An automatic measurement station is designed and implemented to measure and characterize each part of a vibration-based PEH system separately, as well as for the complete system as one module.[44] The designed measurement station allows systematic data acquisition (DAQ) and graphically displays, in near real-time, the characterization data. The station can be utilized for the measurement and comparison of different systems, mechanisms, and designs. The automation of the measurement station and control of all the peripheral equipment, such as the measurement instruments and programmable discrete resistor selector, is achieved using LabVIEW from National Instruments through USB and RS232 interfaces available in all instruments without the need of a signal going through the usual DAQ. The same software (LabVIEW) performs the processing and storage of acquired data including graphically displaying important parameters. This approach makes the characterization processes effective and efficient without operator intervention at every stage.

6.1 Electromechanically parametric characterization of the piezoelectric element

6.1.1 Dielectric characterization

The dielectric constant is one of the most important parameters for the characterization of dielectric materials. It is basically the relative permittivity of dielectric materials. Symbolically, it is denoted by *k* or ε. The dielectric constant for most materials is independent of the electric field strength below a critical field at or above which carrier injection into the material occurs. The dielectric constant strongly depends on the frequency of the AC electric field and on the temperature, pressure, structure, and imperfections of the materials. The dielectric constant or relative permittivity can be expressed as follows:

$$\varepsilon_r = \frac{\varepsilon}{\varepsilon_0}, \tag{25}$$

where ε and ε_0 are the absolute permittivity and vacuum permittivity, respectively. In terms of real and imaginary values, it can be expressed as follows:

$$\varepsilon_r = \varepsilon' - i\varepsilon'', \tag{26}$$

where ε' is the real part of the dielectric constant, and ε'' is the imaginary part called the dielectric loss.

The real part, i.e., the dielectric constant (ε'); the imaginary part, i.e., the dielectric loss (ε''); and the AC conductivity (σ_{ac}) can be determined using

$$\varepsilon' = \frac{C_p A}{\varepsilon_0 d}, \tag{27}$$

$$\varepsilon'' = \varepsilon' \tan\delta, \tag{28}$$

$$\sigma_{ac} = \varepsilon' \varepsilon_0 \omega, \tag{29}$$

where C_p is the parallel capacitance of the sample at a chosen signal frequency ω, $\tan \delta$ is the dielectric loss factor or dissipation factor, A is the electrode area of a silver electrode, ω is the angular frequency, d is the thickness of the sample, and $\varepsilon_0 = 8.854 \times 10^{-12}$ F/m is the permittivity of vacuum.

6.1.2 Electric poling

The total dipole moment per unit volume is called electric polarization. In fact, in polar substances, many atoms and molecules possess a dipole moment, but the net dipole moment becomes zero due to their random orientation canceling the effects of each other. Thus, polarization is crucial before testing to obtain the net dipole moment and thus better dielectric characteristics.

An example poling setup is illustrated in Fig. 16. The electroded samples are poled at room temperature using a voltage of 4 KV with a corona poling setup. After the poling process, the samples are short-circuited and annealed at 50°C for 2 h to remove any extrinsic charges injected during poling.

6.1.3 Pyroelectric coefficient measurement

Pyroelectric materials possess spontaneous polarization in the absence of an external electrical field. The variations in temperature in such a material cause changes in the internal polarization, and a flow of charge occurs. Out of 20 non-centrosymmetric crystals, 10 are pyroelectric and have a unique polar axis. The pyroelectric effect may arise from two contributions: crystal deformation and

Figure 16 A Corona poling setup.

change in temperature. The pyroelectric effect caused by change in temperature, also known as the primary effect, produces a electric displacement in the crystal under constant strain. The secondary pyroelectric effect is caused by crystal deformation due to thermal expansion from the temperature change.[43]

To record the dynamic relative pyroelectric current I_p, the direct method is utilized. The pyroelectric current I_p can be measured at various temperatures at a constant heating rate, and the relative pyroelectric coefficient p is calculated using

$$p = \left(\frac{I_p}{A} / \frac{dT}{dt} \right), \tag{30}$$

where dT/dt is the rate of change of the temperature, which was kept constant throughout the measurement. The change in the pyroelectric coefficient indicates the change in dipole orientation inside the material; the higher the coefficient is, the better the material is for converting temperature change to electrical charge.

6.2 Measurement techniques for the characterization of a piezoelectric energy harvester

When studying the piezoelectric, pyroelectric, ferroelectric, and dielectric properties of materials, knowledge of some electrical parameters, such as impedance, is needed. Impedance is the basic electrical parameter that is used to characterize electronic circuits, components, and materials. It is defined as the ratio of the voltage applied to the device and the resulting current through it. In other words, impedance is the total opposition that a circuit offers to the flow of an AC at a given frequency and is generally represented as a complex quantity that can be shown graphically. The basic elements that make up electrical impedances are inductance, capacitance, and resistance: L, C, and R, respectively. A complex circuit consists of inductance, capacitance, and resistance rather than single components. In the real world, electronic components are not pure resistors, inductors, or capacitors, but a combination of all three. Some of the most important parameters are described in the following sections.

6.3 Parameter identification and piezoelectric coefficients

6.3.1 Mechanical model and equivalent electrical circuit

A mechanically vibrating diagram represents a PEH in an excitation state, which can be presented as a mass-spring-damper system or a single degree of freedom, as illustrated in Fig. 17.[1]

The equation of motion of the previous model can be described using Newton's second law as follows:

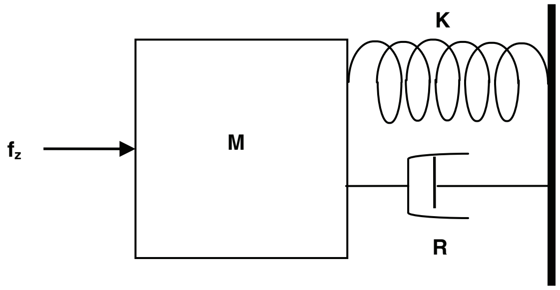

Figure 17 Single-degree-of-freedom mechanical model.

$$f_z = f_M + f_R + f_K, \tag{31}$$

where f_z is the external force, f_M is the inertial force, f_R is the frictional force, and f_k is the elastic force. Equation (31) can be written using its differential form as follows:

$$f_z = M\frac{d^2x}{dt^2} + \mathbf{R}\frac{dx}{dt} + \frac{1}{k}x = M\frac{dv}{dt} + \mathbf{R}v + \frac{1}{k}\int_0^t v d\tau. \tag{32}$$

Assuming that the external force is a sinusoidal excitation force ($f_z = f \sin \omega t$), Eq. (32) can be rewritten as follows:

$$\bar{f}_z = f_z e^{i\omega t} = i\omega M\bar{v} + \mathbf{R}\bar{v} + \frac{1}{i\omega k}\bar{v}. \tag{33}$$

The complex mechanical impedance of the transducer thus equals

$$Z_{\text{mech}} = \frac{\bar{f}_z}{\bar{v}} = i\omega M + \mathbf{R} + \frac{1}{i\omega k} = \mathbf{R} + i\left(M\omega - \frac{1}{\omega k}\right) = Z_{\text{mech}} e^{i\phi}. \tag{34}$$

The impedance module equals

$$Z_{\text{mech}} = \sqrt{\mathbf{R}^2 + \left(M\omega - \frac{1}{\omega k}\right)^2} = \sqrt{\mathbf{R}^2 + X^2}, \tag{35}$$

$$\phi = \tan^{-1}\left(\frac{X}{\mathrm{R}}\right). \tag{36}$$

A typical equivalent series electrical circuit for Eq. (36) can be modeled at resonance, as shown in Fig. 18.

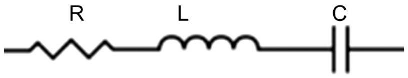

Figure 18 Equivalent series electrical circuit model.

The impedance of the equivalent circuit in Fig. 18 can be described as follows:

$$Z_m = i\omega L + R + \frac{1}{i\omega C} = R + i\left(\omega L - \frac{1}{\omega C}\right). \tag{37}$$

The governing differential equation can be found by substituting into Kirchhoff's voltage law the constitutive equation for each of the three elements in Fig. 18 as follows:

$$V_R + V_L + V_C = V(t), \tag{38}$$

where V_R, V_L, and V_C are the voltages across R, L, and C, respectively, and $V(t)$ is the time-varying voltage from the source. Substituting into the constitutive equations, we obtain Eq. (39):

$$Ri(t) + L\frac{di(t)}{dt} + \frac{1}{C}\int_{-\infty}^{t} i(\tau)d\tau = V(t). \tag{39}$$

According to Eq. (39), an electric charge is proportional to the deformation as follows:

$$f_z = k_p V \tag{40}$$

and

$$q = k_p x. \tag{41}$$

The electrical current is defined as follows:

$$i = \frac{dq}{dt} = k_p\frac{dx}{dt} = k_p v. \tag{42}$$

From Eq. (43), it is shown that

$$v = \frac{i}{k_p}. \tag{43}$$

After substituting Eqs. (42) and (43) into Eq. (33), the result can be written as follows:

$$k_p V = \frac{M}{k_p}\frac{di}{dt} + \frac{\mathbf{R}}{k_p} i + \frac{1}{K k_p}\int_{-\infty}^{t} i(\tau)d\tau. \tag{44}$$

Then,

$$V = \frac{M}{k_p^2}\frac{di}{dt} + \frac{\mathbf{R}}{k_p^2} i + \frac{1}{K k_p^2}\int_{-\infty}^{t} i(\tau)d\tau. \tag{45}$$

By comparing Eq. (39) with Eq. (41), one can see that

$$L = \frac{M}{k_p^2}, R = \frac{\mathbf{R}}{k_p^2}, C = k_p^2 K. \tag{46}$$

6.3.2 Linear piezoelectric model

The electrical circuit representing an oscillating piezoelectric element of Eq. (39) is shown in Fig. 18. Figure 19 demonstrates two additional electrical components, C_e and R_e, which represent the electrical capacitance and resistance of the piezoelectric element, respectively. An object of mass vibrating with a certain range of frequencies exhibits high peak values called the resonant frequency f_r. This resonant frequency is followed by an antiresonant frequency (f_a), where the impedance of the body is at a maximum and the oscillation amplitude is at a minimum. A typical resonance plot of impedance versus frequency for a piezoelectric ceramic near resonance is shown in Fig. 20. Notice the resonant frequency f_r at the point of minimum impedance and the antiresonant frequency f_a at the point of maximum impedance.

6.3.3 Electromechanical coupling coefficients

The electromechanical coupling coefficient numerically measures the conversion efficiency between the electrical and acoustic energies in piezoelectric materials.

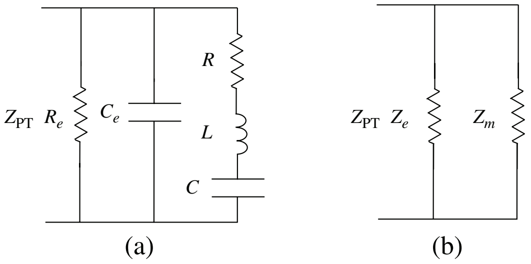

Figure 19 Linear piezoelectric transducer Z_{PT}, electrical impedance of the transmitter: (a) a detailed diagram and (b) the distribution of the branches of electrical and mechanical.

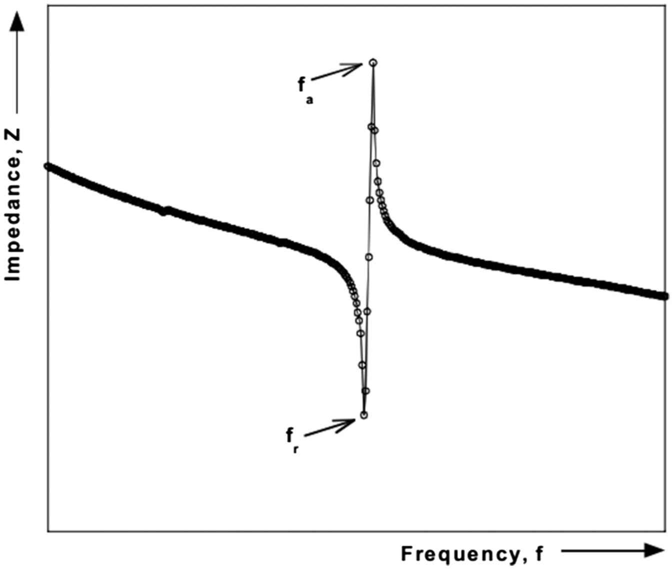

Figure 20 Impedance of a piezoelectric ceramic at resonance f_r at the point of minimum impedance and the antiresonant frequency f_a at the point of maximum impedance.

Some of the most often used electromechanical coupling coefficients are k_p, k_{31}, and k_{33}. Subscripts p, 31, and 33 represent planar, length extensional, and thickness extensional modes, respectively. The coefficients k_{33} and k_{31} are calculated from the frequencies of minimum f_r and maximum impedances f_a, as shown previously in Fig. 20, and are given by the following equation:[23]

$$k_{31}^2 = \frac{\Psi}{(1+\Psi)}, \tag{47}$$

where

$$\begin{aligned} \Psi &= \frac{\pi}{2}\left(1+\frac{f_a - f_r}{f_r}\right)\tan\left[\frac{(f_a - f_r)}{2f_r}\right], \\ k_{33}^2 &= \frac{\frac{\pi}{2}}{1+\frac{(f_a - f_r)}{f_r}}\tan\left[\frac{\frac{\pi(f_a - f_r)}{2f_r}}{1+\frac{(f_a - f_r)}{f_r}}\right], \end{aligned} \tag{48}$$

and the planar coupling coefficient is given as follows:

$$k_p = \frac{f_a^2 - f_r^2}{f_r^2}. \tag{49}$$

6.3.4 Elastic compliance

The strain produced in a piezoelectric material per unit stress applied is called the elastic compliance. For example, an elastic compliance S_{11}^{E} represents stress due to a constant electric field in the direction perpendicular to the polarization direction of the ceramic element (in direction 1) with strain in direction 1. S_{33}^{E} denotes that electric compliance is produced by stress in the direction parallel to which the ceramic element is polarized (in direction 3) with strain in direction 3 under the application of a constant electric field (open circuit).[24] An equation[23] for finding the elastic constant of a piezoelectric element can be expressed as follows:

$$s_{33}^{D} = \frac{1}{4\rho f_a^2 l^2}, \tag{50}$$

$$s_{33}^{E} = \frac{s_{33}^{D}}{1 - k_{33}^2}, \tag{51}$$

$$s_{11}^{E} = \frac{1}{4\rho f_r^2 w^2}, \tag{52}$$

$$s_{11}^{D} = s_{11}^{E}(1 - k_{31}^2), \tag{53}$$

where ρ is the density of the material in kg/m^3, l is the distance between electrodes, and w is the width of the ceramic. The superscripts D and E stand for constant electric displacement (open circuit) and constant electric field (short circuit), respectively.

6.3.5 Piezoelectric charge constants

The mechanical strain S experienced by piezoelectric materials per unit of electric field is defined as the piezoelectric charge constant. The mathematical relations for calculating piezoelectric charge constants are as follows:

$$d_{31} = k_{31}\sqrt{\varepsilon_0 K_3^T s_{11}^E}, \tag{54}$$

$$d_{33} = k_{33}\sqrt{\varepsilon_0 K_3^T s_{33}^E}, \tag{55}$$

where K_3^T is the free-relative dielectric constant, and ε_0 is the permittivity of free space.

6.3.6 Piezoelectric voltage constant

The piezoelectric voltage constant is defined as the mechanical strain experienced by a piezoelectric material per unit electric displacement. In other words, the electric field is generated by a piezoelectric material per unit of mechanical stress applied. The g_{ij} piezoelectric constants are related to the d_{ij} coefficients by the following equations:[24]

$$g_{31} = \frac{d_{31}}{\varepsilon_0 K_3^T}, \tag{56}$$

$$g_{33} = \frac{d_{33}}{\varepsilon_0 K_3^T}. \tag{57}$$

6.3.7 Mechanical quality factor

The mechanical quality factor Q_M is defined as the ratio of reactance to resistance in the series equivalent circuit of Fig. 19(b) and is given by[23]

$$Q_M = \frac{1}{2\pi f_r Z_m C_o}\left(\frac{f_a^2}{f_a^2 - f_r^2}\right). \tag{58}$$

It is important that more accurate new experimental and instrumental methods are being constantly developed with improvements in the old ones. A detailed description of the experimental equipment employed in these methods is not possible. An effort has been made to give a brief introduction to the physical ideas and concepts of experimental methods together with the instruments.

6.3.8 Dielectric constants and dielectric spectrum measurements at a low frequency

The dielectric constant and dielectric loss are important practical parameters for most applications of ferroelectric materials. In ferroelectric materials, the study of the dielectric properties provides a great deal of information for understanding the molecular structure and the mechanisms of electric polarization. The most extensively used method to measure ε' (C_p) and tan δ is the electric bridge method. For this purpose, several bridges with different circuits can be utilized with their frequencies covering a range from 0.01 Hz to 150 MHz. Commercially, more than 10 different models of digital vector impedance analyzers are available. A typical setup for the measurement of dielectric constants and the pyroelectric coefficient is shown in Fig. 21.[27,28] Those shown can measure more than 10 electrical parameters very efficiently and are usually easy to use.

6.3.9 Polarization (hysteresis loop) measurements

Generally, a linear capacitance is placed in series with the device under test (DUT) for polarization measurement and an AC or DC voltage is applied. The polarization of the sample is equivalent to the voltage measured across the capacitor. For measuring a spontaneous polarization of the order of 5 to 50 $\mu\mathrm{Ccm}^{-2}$ in bulk samples, a voltage >1000 V is required. In the presence of an applied field, this circuit is used to measure a ferroelectric hysteresis loop, that is, the material's

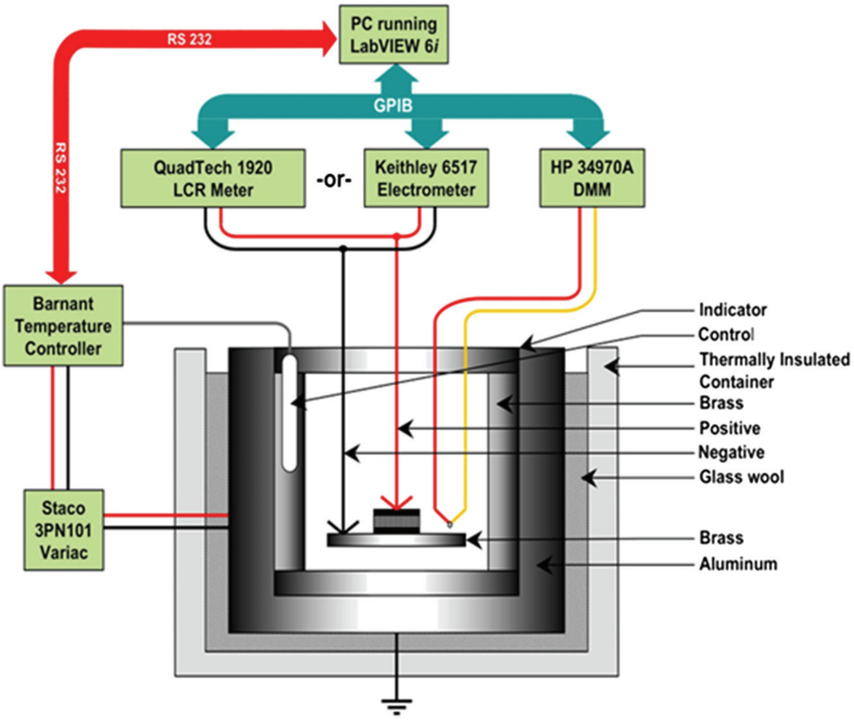

Figure 21 A typical setup for the measurement of dielectric constants and a pyroelectric current.

switchability (Fig. 22). By measuring the polarization of the material in μCcm^{-2} as a function of the applied voltage V, the hysteresis loop is determined. Different points of the hysteresis loop of interest include the spontaneous polarization P_s and remnant polarization P_r, the coercive field E_c, and the general shape of the loop (Fig. 23).[29]

The condition in which polarization will not increase with applied voltage is the saturation state of the material, and all the dipole moments are unidirectional.

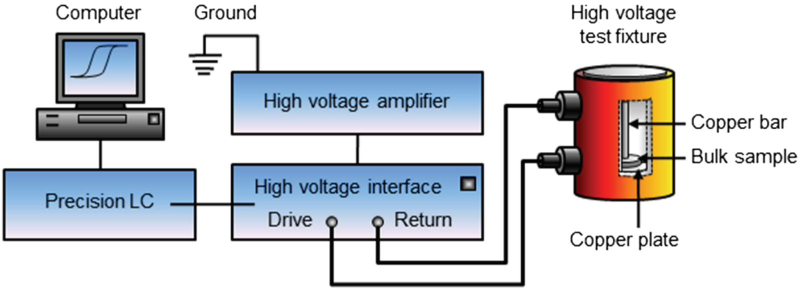

Figure 22 Block diagram of a commercial sawyer-tower setup.

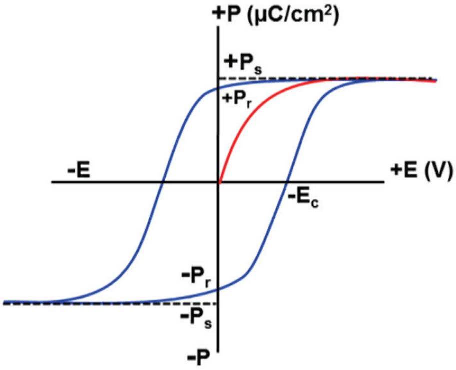

Figure 23 Ferroelectric hysteresis loop (polarization vs. applied voltage).

The spontaneous polarization $+P_s$ is represented by linear extrapolation of the curve back to the polarization axis. Some dipole moments will remain aligned, and a remnant polarization P_r is observed as the applied voltage is reduced from its maximum positive value to zero. As the applied voltage spans the range from its maximum positive to negative, $-P_s$ and $-P_r$ will be observed.

Further information provided by the ferroelectric hysteresis loop includes the coercive field E_c and the shape of the loop. The E_c represents the magnitude of the external field applied voltage necessary to remove all polarization from the material. The E_c and the shape of the loop (or sharpness) are influenced by grain size and homogeneity, and they depend upon sample preparation.

6.3.10 Determination of piezoelectric coefficients

An experimental technique employed to measure the piezoelectric ($\overline{d}_{33}$, $\overline{d}_{31}$, and $\overline{k}_{33}$) and mechanical properties ($\overline{s}^E_{33}$ and $\overline{s}^D_{33}$) is described in detail.[1] The principles of each measurement method and its application to test the DUT are introduced and discussed in the following sections.

To evaluate the $\overline{d}_{33}$ and $\overline{d}_{31}$ coefficients of the piezoelectrics, a "take-control" piezometer is used. The system uses the direct piezoelectric effect, that is, a charge generation with an applied load, to measure the piezoelectric coefficients. Berlincourt developed this technique for the first time (hence why it is named after him). The system setup is shown in Fig. 24.

The piezometer consists of a digital display unit, which displays the measurements, and upper and lower loading arms, which apply the load and measure the charge generated from the sample. The upper loading arm can be moved vertically on the screw-threaded pillars by rotation of the loading arm handle. The lower loading arm is spring-loaded and vibrates in the vertical plane at a frequency of 97 Hz, applying a sinusoidal force of ~0.1 N to the sample through mechanical contact. This oscillatory force is in addition to the static preload that is applied by rotation of the upper-loading-arm handle. Various studs can be

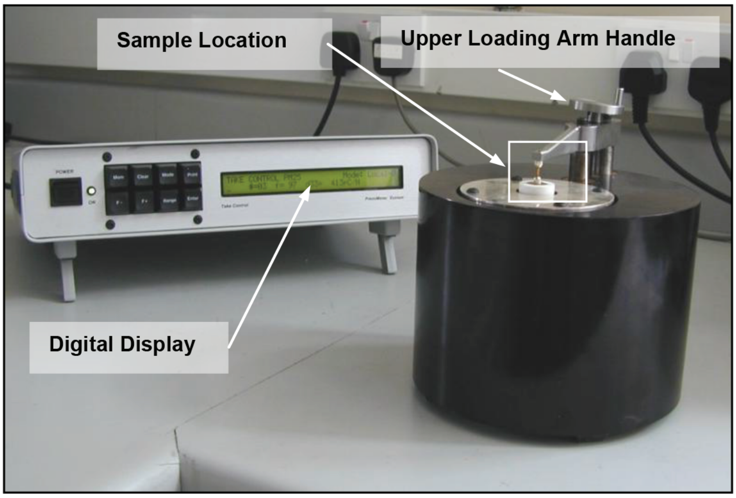

Figure 24 The take-control piezometer system (setup shown for measuring d_{33}).

screwed into the upper and lower loading arms in the "sample location" section of Fig. 24, which depends on the sample size and the measurement being made (d_{33} or d_{31}). An expanded and labeled view of this location setup for measuring d_{33} and d_{31} is shown in Figs. 25(a) and 25(b), respectively.

For evaluation of $\overline{d}_{33}$, conducting metal studs are screwed into the upper and lower loading arms, and the sample is positioned between the two studs with the three-direction in the vertical plane, as shown in Fig. 25(a). The upper-loading arm-handle is turned to bring the studs into mechanical and electrical contact with

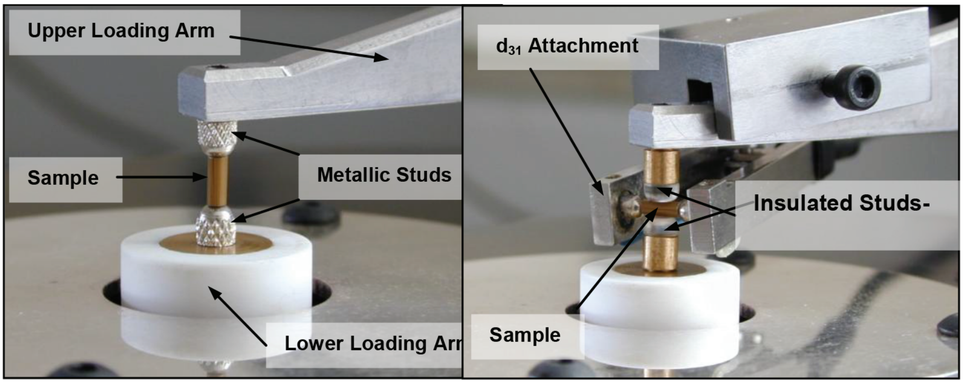

(a) (b)

Figure 25 The piezometer "sample test location" showing measurement of (a) d_{33} and (b) d_{31} for a 1-to-3 composite.

the sample's electroded end faces. The handle is then rotated one full turn to apply a 10-N preload to the sample by depression of the spring-loaded lower loading arm. In this case, the force is applied parallel to the poling direction, and the charge generated by the sample is collected through the studs and is used to calculate $\bar{d}_{33}$. In this case, $\bar{d}_{33}$ is measured as the charge produced per unit applied force ($\mathrm{C\ N^{-1}}$).

To evaluate $\bar{d}_{31}$, the metallic studs are replaced with non-conducting polymer-tipped studs. The sample is positioned between the studs with the three-direction in the horizontal plane and the upper-loading-arm handle is turned so that the studs make mechanical contact in the one-direction. The handle is turned one full turn to apply a 10-N preload to the sample through the spring loaded lower loading arm. In this case, the force is applied normal to the poling direction. The charge generated on the electroded ends of the sample is collected by a special d_{31} attachment that is attached in a position on the upper loading arm. This test setup is shown in Fig. 25(b).

6.3.11 Impedance analysis for the measurement of $\bar{s}^E_{33}$, $\bar{s}^D_{33}$, and $\bar{k}_{33}$

The impedance analysis technique is used to determine the $\bar{s}^E_{33}$, $\bar{s}^D_{33}$, and $\bar{k}_{33}$ of the composites.[1] A body will exhibit several modes of vibration. Piezoelectric materials are unique in that mechanical resonance can be induced by applying an AC voltage across the sample. When the electrical drive frequency coincides with a mechanical resonance of the sample, an impedance minimum occurs (Fig. 26). Conversely, when the electrical drive frequency coincides with a mechanical antiresonance of the sample, an impedance maximum occurs. The frequency of the resonance and antiresonance modes is governed by the sample dimensions, density, and various piezoelectric, dielectric, and mechanical coefficients. Therefore,

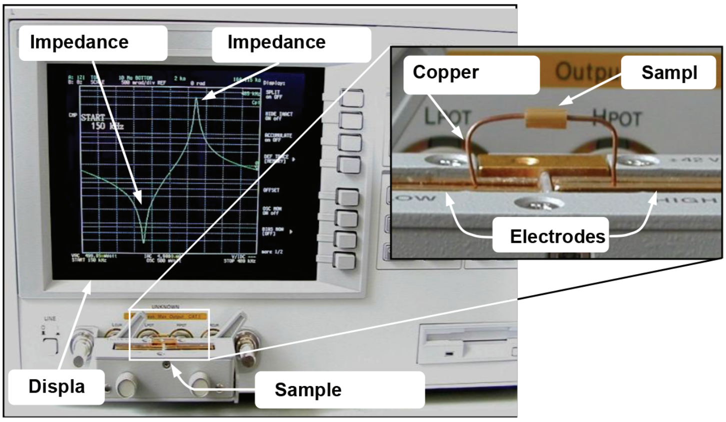

Figure 26 Test setup for impedance spectroscopy of 1-to-3-geometry composites. The impedance vs. frequency curve generated on the display is typical of a high-volume, fraction composite response.

with knowledge of the impedance response of a sample, it is possible to calculate various piezoelectric and mechanical coefficients. Equations appropriate for the longitudinal-length mode are given in Eqs. (45) and (49) in which l and ρ are the sample length and density, and f_r and f_a are the resonance and antiresonance frequencies, respectively:

$$s_{33}^{D} = \frac{1}{4\rho f_s^2 l^2}, \tag{59}$$

$$s_{33}^{E} = \frac{s_{33}^{D}}{1 - k_{33}^{2}}, \tag{60}$$

$$k_{33} = \left[\frac{\pi f_r}{2 f_a} \cot\left(\frac{\pi f_r}{2 f_a}\right)\right]^{1/2}. \tag{61}$$

To evaluate the $\bar{s}_{33}^{D}$, $\bar{s}_{33}^{E}$, and $\bar{k}_{33}$ coefficients of the composites, the impedance of the sample can be measured using an Agilent 4194A impedance analyzer. The experimental setup, which shows a typical impedance spectrum being generated on the analyzer display, is shown in Fig. 26. An expanded view of the sample test location is also shown.

Two thin copper wires were attached to the low and high electrodes to allow connection to the sample. Because this test setup is not a standard fixture, compensation is performed for both open- and short-circuit conditions in accordance with the procedure in the Agilent 4194A instruction manual. Open-circuit conditions were enforced by ensuring that no sample is loaded between the copper wires, while short-circuit conditions are enforced by loading a copper sample, with similar dimensions to the composites, into position between the wires. Once fixture compensation had been performed, samples were positioned between the copper wires in preparation for testing. Care was taken not to allow the wires to clamp the samples too strongly because this would force deviation from the "mechanically free" boundary conditions required by the test method. Once loaded, the impedance is measured over the frequency range of 150 to 500 kHz with an excitation voltage of 500 mV. The maximum and minimum impedance values, and the corresponding frequencies at which they occurred, are recorded. These values are used in Eq. (4.61) to calculate the relevant material properties.

6.3.12 Pyroelectric coefficient measurements

The determination of the pyroelectric coefficients is divided into two parts: the measurement of the pyroelectric current and the measurement of the charge generated.

The pyroelectric effect can be sub-divided into primary and secondary effects. The primary effect is observed when the sample is rigidly clamped under a constant strain to prevent any thermal expansion or contraction. Secondary effects occur when the sample is permitted to deform, that is, the material is under constant stress. Thermal expansion results in strain that changes the spontaneous polarization attributable to the piezoelectric effect. Thus, the secondary pyroelectric effect includes contributions caused by piezoelectricity. Exclusive measurements of the pyroelectric coefficient under constant strain is experimentally very difficult. What is experimentally measured is the total pyroelectric effect exhibited by the material: the sum of the primary and secondary effects.

The pyroelectric current I_p was measured at various temperatures at a constant heating rate, and the relative pyroelectric coefficient p was calculated using the following relationship:

$$p = \left(\frac{I_p}{A} / \frac{dT}{dt}\right), \tag{62}$$

where dT/dt is the rate of change of temperature, which was kept constant throughout the measurement. The change in pyroelectric coefficient indicates the change in dipole orientation inside the material; the higher the coefficient is, the better the material is for converting temperature change into electrical charge. The details of the measurements are described in other publications.[43]

The pyroelectric charge integration method, also known as the static method, determines the charge, that is, polarization, of the sample as a function of the temperatures. The technique works very well at discrete temperatures. The static method was "glass," with an integration method that allowed for larger changes in temperature.[43] For a temperature change in pyroelectric, charges on the electrodes of the sample are

$$\Delta Q = A\left(\frac{dP_s}{dT}\right)\Delta T. \tag{63}$$

Therefore, the total change in charge as the temperature changes from $T1$ to $T2$ is as follows:

$$\int \Delta Q = A\int_{T1}^{T2}\left(\frac{dPs}{dT}\right)\Delta T = A[\Delta P]_{T1}^{T2}. \tag{64}$$

By using an operational amplifier with a feedback capacity C, the output voltage V_{SC} of this amplifier is found to be directly proportional to the integral of the input current, that is,

$$V_{\mathrm{SC}} \approx -(1/C)\int Isdt = -(A/C)[\Delta P]_{T1}^{T2}. \tag{65}$$

The pyroelectric current is obtained from the slope of the curve $V_{\mathrm{SC}}(T)$.

6.4 Parametric identification and determination for a piezoelectric energy harvester

The most common PEH is the cantilever structure. The dynamic model of the harvester depends on several parameters, such as the physical dimensions and the mechanical and electrical properties of the material. In many cases, not all of the information about these parameters are available, which causes difficulties in developing a theoretical model for analysis and simulation. Model parameters for cantilever mechanical structures are identified experimentally to reduce the required modeling efforts. The PEH testing system is described in Fig. 28 with all of the instruments.[44] The performance of an energy-harvesting device is often characterized by the measurement of its electrical output under a specified set of conditions, for example, specification of input acceleration amplitude (base amplitude) and measurement of electric output into a known resistive load.

However, even with a relatively simple setup, the performance characteristics depend in a complex way on base acceleration amplitude, load resistance, and the design of the energy harvester. The harvested power for a vibrating cantilever/tip mass depends upon both the frequency and the amplitude of vibration. Such performance measurements can be used to map out the characteristics of the system and compare them to models to implement optimization strategies to maximize performance. However, they do not provide direct information on the energy transfer and losses within the system. An important parameter in this respect is efficiency, which is defined as the ratio of energy or power OUT to energy to power IN to the energy harvester. Piezoelectric harvester efficiency can, in theory, approach 100%. A small harvester attached to a large inertial vibration source does not significantly load the vibrating system, and energy drawn from the system is small. However, the overall system performance can be boosted by improving the efficiency, particularly when other design constraints, such as the vibrating volume, are considered. Piezoelectric vibration harvesters generate charge from strain in a piezoelectric material created by the inertia of a suspended mass undergoing acceleration. This is commonly achieved using a piezoelectric cantilever, as shown in Fig. 22. A bimorph construction employs a symmetrical arrangement of the piezoelectric material around the neutral axis, creating strain.

6.4.1 Natural frequency identification

The resonance (natural) frequency of the cantilever harvester can be detected by tracking the maximum power or the maximum open-circuit voltage.[1] At this frequency, the harvester produces the maximum power output. The following procedure can be used to experimentally detect the natural frequency by maximum power tracking: the output voltage from the harvester is connected to an electrical resistance load R; the system is excited at the retained frequency ω with a fixed vibration amplitude; measure the output voltage V on the resistive load and compute the power output to the load as V^2/R. This step is repeated at different frequencies. By drawing the relationship between the power outputs versus the excitation frequency, the maximum power indicates the natural frequency.

6.4.2 Damping factor identification

The damping factor η can be identified by observing the harvester impulse response. The magnitude of the oscillations is measured at two separate points (x_1, x_2), n periods apart, as illustrated in Fig. 27.

The damping ratio can then be calculated as a function of the natural frequency of the natural log decrement of the two magnitudes and the number of damped periods n, as shown in Eq. (66). For accurate determination of the damping coefficient, the calculation can be repeated with different damping periods n and then take the average value:

$$\eta = \frac{1}{2\pi n} \ln \frac{x_1}{x_2}. \tag{66}$$

6.4.3 Quality factor identification

The harvesting cantilever must be selected with a high Q-factor to increase the output power. A higher Q-factor indicates a lower rate of energy loss relative to the stored energy. However, a high Q-factor also means a narrow operational frequency bandwidth. The harvester will only produce significant power while working under an excitation frequency that closely matches its resonant frequency. The total quality factor Q can be computed as the ratio between the resonance frequency f_n and the frequency bandwidth f_{bw} as follows:

$$Q = \frac{f_n}{f_{bw}}, \tag{67}$$

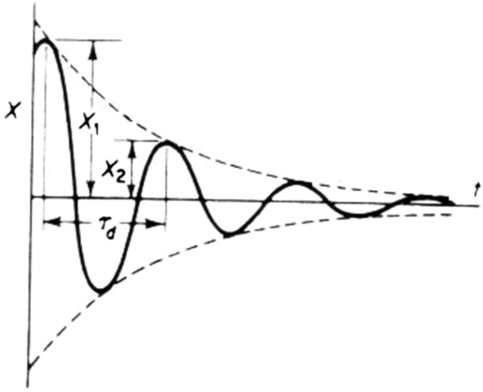

Figure 27 Damped oscillation using an impulse force input.

where the frequency bandwidth is the width of the range of frequencies for which the energy is at least half its peak value. The quality factor is inversely proportional to the damping factor, which is given by

$$\eta = \frac{1}{2Q}. \tag{68}$$

It is evident that if the quality factor is known, the damping factor can also be calculated by the above equation.

6.4.4 Efficiency of energy conversion

The efficiency of energy conversion η is described at resonance as

$$\eta = \frac{k^2/[2(1-k^2)]}{1/Q + k^2/[2(1-k^2)]}, \tag{69}$$

where k is the electromechanical coupling factor, and Q is the quality factor.

6.5 Architecture of a piezoelectric energy-harvesting station

The test station was set up as shown in Fig. 28.[55] The experimental setup consists of a small mechanical shaker (Bruel and Kjaer Model Type 4810) and a function generator (Agilent/Keysight 33500B) to produce a range of vibration frequencies and a high-power amplifier (Bruel and Kjaer Model 2718) to create the cyclic force of the required magnitude and frequency. Accelerometer sensors were employed to measure the vibration acceleration (the sensitivity of the accelerometer sensor is 100 mV/g). A multimeter (Keithley Model 2110) was used to measure the output voltage from the harvester, and a laser displacement meter (MTI Model Microtrack II) was used to measure the displacement of the cantilever beam. An IET PRS-2000 programmable resistance substituter (PRS) was used to add an electrical load to the harvester circuit. The DAQ of the acceleration sensors was achieved with a picoscope (Pico-Technology Model 4224). To avoid any interference from the noise in the surrounding environment, all of the experiments were performed on an isolated optical bench. When the piezoelectric harvester was subjected to vibrations by the experimental setup, it produced an AC electrical output, and the output signal from the harvester was connected to a programmable resistance selector or an AC–DC circuit with a capacitive load.

LabVIEW software (National Instruments Inc.) is installed on the computer to act as the controlling center for the system, and it is used to set the exciting frequency to the arbitrary waveform generator (AWG), to assign the reading type of the multimeter, and to record the data through a USB interface. One end of the cantilever beam is fixed in a fixture attached to the shaker. A small mass can be attached on the other end of the cantilever beam to tailor the resonant

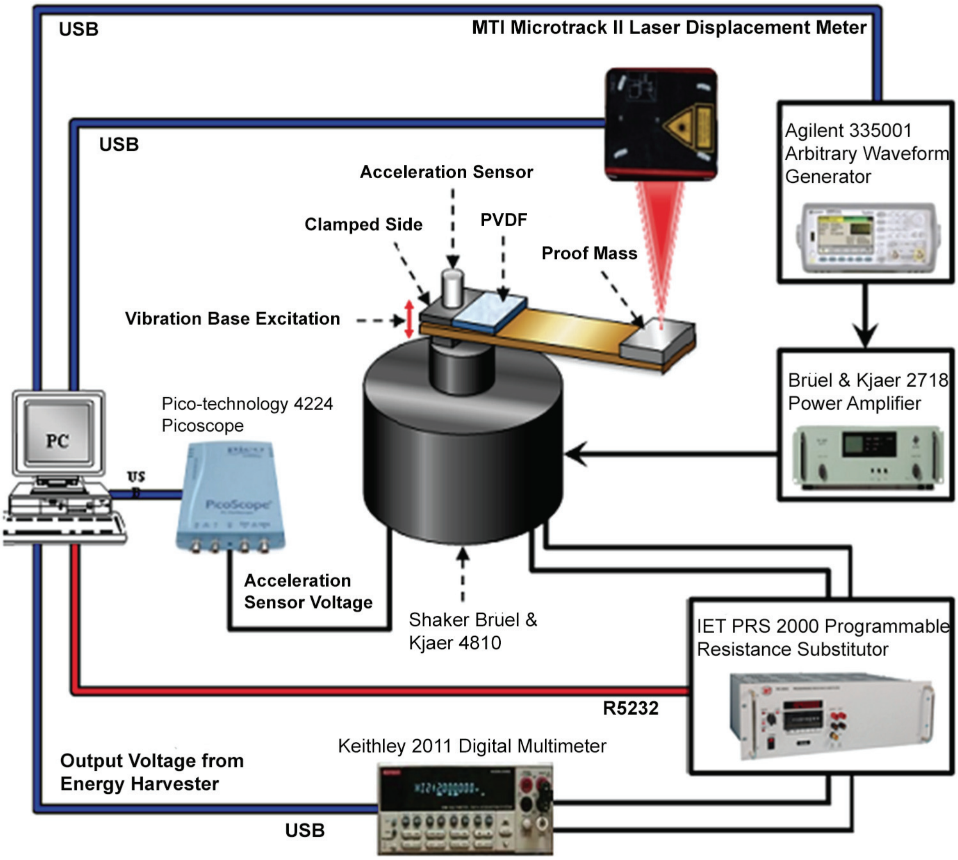

Figure 28 A configuration of the test station for a vibration-based energy harvester.

frequency of the harvester. A pair of wires is used to conduct the produced current through the programmable resistive load.

6.5.1 Instrument specifications and manufacturers

Table 6 lists the complete description of all instruments utilized in the station. When the piezoelectric harvester is subjected to vibrations by the experimental setup, it produces an AC electrical output, and the output signal from the harvester is connected to a programmable resistance selector or an AC–DC circuit with a capacitive load. Figure 29 shows the sample holders for discrete parameter determinations.

6.6 Procedure for output voltage versus frequency measurements

The test station setup is shown in Fig. 30.[55] After turning on all of the measurement instruments and setting up the amplitude of excitation by controlling the power amplifier, the LabVIEW software is initiated. The block diagram of the

Table 6 Detailed description of instruments utilized in the PEH station.

Instrument	**Specification**
Keithley 2110 Display DMM www.keithley.com	Speed: 200 readings/s through USB interface DC voltage range: 100 mV Resolution: 1 μV Accuracy: ±0.012% Resistance: ±0.020% 1 year Input resistance: 10 MΩ
Agilent 33250B Function/AWG www.keysight.com	Amplitude accuracy (at 1 kHz, >10 mV_{pp}), Autorange on: ±1% of setting ± 1 mV_{pp}
Brüel and Kjær Type 4810 Mini-Shaker www.bksv.com	Force rating (peak): 10 N, 65 Hz to 4 kHz 7 N, 65 to 18 Hz Frequency range: DC to 18 kHz Maximum displacement (peak to peak): 4 mm Maximum bare table acceleration (peak): 550 m/s^2 (65 Hz to 4 kHz) 383 m/s^2 (6.5 to 18 kHz) 1 $m/s^2 = 0.102$ g
Brüel and Kjær Type 2718 Power amplifier www.bksv.com	Voltage RMS read-out accuracy: ±3% ± 1 digit, 50 Hz to 20 kHz Current RMS read-out accuracy: ±3%, adjustable ±1 digit, 50 Hz to 20 kHz
IET Labs PRS-200 PRS www.ietlabs.com	Resistance range: 0 to 9,999,999 Ω Accuracy: ±(1% + 70 mΩ) Resolution: 1 Ω

Pico technology PicoScope 4224 IEPE Oscilloscope www.picotech.com	Voltage range: ±50 mV to ±20 V in nine ranges Input impedance: 1 MΩ Sensitivity: 10 mV/div to 4 V/div DC accuracy: 1% full scale Time base: 100 ns/div to 5000 s/div Time base accuracy: 50 ppm Vertical resolution: 12 bits
MTI Instruments MICROTRAK II Laser displacement sensor www.mti-instruments.com	Range: ±1 mm Resolution: ±0.12 μm Laser spot size: 20 μm Laser angle: 45 deg
QuadTech 1920 LCR bridge www.ietlabs.com	20 Hz to 1 MHz frequency range, 27,000 possible frequency options 0.1% basic measurement accuracy Test frequency accuracy: ±0.02% + 0.02 Hz
Keithley 6517B Electrometer www.keithley.com	Electrometer/high resistance meter, 100 aA to 20 mA, 10 μV to 200 V, 100 Ω to 10 PΩ 10 aA (10 × 10 to 18 A) current measurement resolution Less than 3 fA input bias current 5 1/2-digit high-accuracy-measurement mode
Point laser vibrometer www.omscorporation.com	Velocity range: 5 μm/s to 800 mm/s Displacement range: 50 pm to 100 mm Laser: 650 nm Frequency range: DC to 20 kHz
Acceleration transducer www.bright-eng.com	Acceleration range: 490 m/s^2 (50 g) peak overall acceleration within the 10 Hz to 15 kHz frequency span Amplitude linearity: ±1% to 490 m/s^2 (50 g) peak Sensitivity: 2.5 mV/m/s^2 (25 mV/g) ±5%

Table 6 continued

Instrument	**Specification**
Precision LC www.ferrodevices.com	Voltage range (built-in drive voltage): ±500 V built-in Minimum charge resolution: <10 fC Maximum charge resolution: 276 μC Maximum hysteresis frequency: 5 kHz at 10 V Minimum hysteresis frequency: 0.03 Hz
Infrared heat source/bulb www.westinghouselighting.com	Energy used (W)..........................250 Domestic code.............................250R40/HT Volts...120 Beam type...................................Flood Filament type...............................C9 Light center length (LCL)............ 4 in. Average rated hours.....................5000 Life (in years)...............................4.6
Non-contact thermometer www.amazon.com	Resolution: 0.1°C

1. Oscilloscope; 2. Wave-form Generator; 3. Multimeter; 4. Programmable Resistor 5. Power Amplifier; 6. Vibrometer; 7. Laser Displacement Meter; 8. Piezoelectric Cantilever; 9. Shaker

Figure 29 Photographs of sample holders.

Figure 30 A photograph of the experiment test setup showing all necessary components: (1) oscilloscope, (2) waveform generator, (3) multimeter, (4) programmable resistor, (5) power amplifier, (6) vibrometer, (7) laser displacement meter, (8) piezoelectric cantilever, and (9) shaker.

PEH program and the designed front LabVIEW panel screen are illustrated in Fig. 31. Then the following programming order of operations are followed, as described below, to record the vibrating frequency of the cantilever, output AC voltage, and respective resistance.

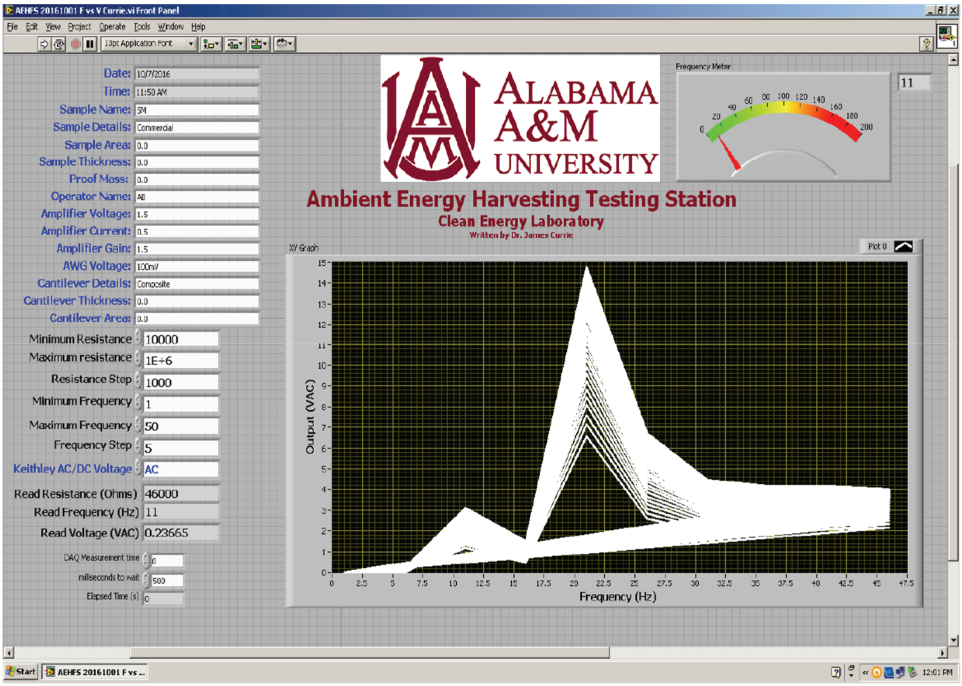

Date: 10/7/2016
Time: 11:50 AM
Sample Name: SM
Sample Details: Commercial
Sample Area: 0.0
Sample Thickness: 0.0
Proof Mass: 0.0
Operator Name: AB
Amplifier Voltage: 1.5
Amplifier Current: 0.5
Amplifier Gain: 1.5
AWG Voltage: 100mV
Cantilever Details: Composite
Cantilever Thickness: 0.0
Cantilever Area: 0.0
Minimum Resistance 10000
Maximum resistance 1E+6
Resistance Step 1000
Minimum Frequency 1
Maximum Frequency 50
Frequency Step 5
Keithley AC/DC Voltage AC
Read Resistance (Ohms) 46000
Read Frequency (Hz) 11
Read Voltage (VAC) 0.23665
DAQ Measurement time 0
miliseconds to wait 500
Elapsed Time (s) 0

Figure 31 A screenshot of the control panel of the LabVIEW program.

The program order of execution is as follows. The first step is to enter the sample information into the control string boxes that will be recorded in the header of the data file. The next step is to select the resistances, frequencies, and other parameters for the system which will also be recorded in the data file. The starting, ending, and resistance steps are selected. The starting, ending, and frequency steps are selected. The AC or DC voltage measurement is selected. A wait time between the measurements is selected. The next step is to run the program, which can be initiated by selecting the arrow icon or simultaneously depressing <Ctrl> <R>. The program will ask to find the "test001.txt" file, which is located on the desktop. As the program is executed, the Agilent 33500B AWG, the IET PRS-2000 PRS, and Keithley 2011 digital multimeter (DMM) are initialized. Next, a series of nested do loops are executed. In the level-1 do loop, a resistance value is sent to the PRS. The value is iterated until the maximum value is encountered, then a "false" Boolean is generated, and the do loop stops. In the level-2 do loop, a frequency value is sent to the AWG. The value is iterated until the maximum value is encountered, then a "false" Boolean is generated, and the do loop stops. In the level-3 do loop, the voltage is measured from the DMM. Data are updated and recorded. The resistance, frequency, and voltage are written to the data file. Data are updated on the front panel. The resistance is displayed on the digital read out; the frequency is displayed on the digital read out and meter; and the voltage is displayed on the digital read out. Frequency versus voltage is plotted on an *XY* graph. The voltage measurement continues until a timeout is encountered, then a "false" Boolean is generated, the do loop stops, and the program jumps to the level-1 do loop. When a "blank" character string is encountered, the outer loop stops, the AWG output is turned off, and the PRS is programmed to 0 Ω. The program ends, and then the user should locate the file "test001.txt" and rename it.

6.7 Procedure for obtaining output voltage versus resistance measurements

The test station is set up, as shown in Fig. 28. After turning on all measurement instruments and setting up the amplitude of excitation manually using the control on the power amplifier, the LabVIEW software is initiated. The designed front LabVIEW panel screen is illustrated in Fig. 32. LabVIEW is used to perform a series of predetermined sweeps; each sweep is performed with a preselected resistive load using a programmable resistance selector to PEH. Then the following programming order of operations are followed, as described below, to record the vibrating frequency of the cantilever, output AC voltage, and respective resistance.

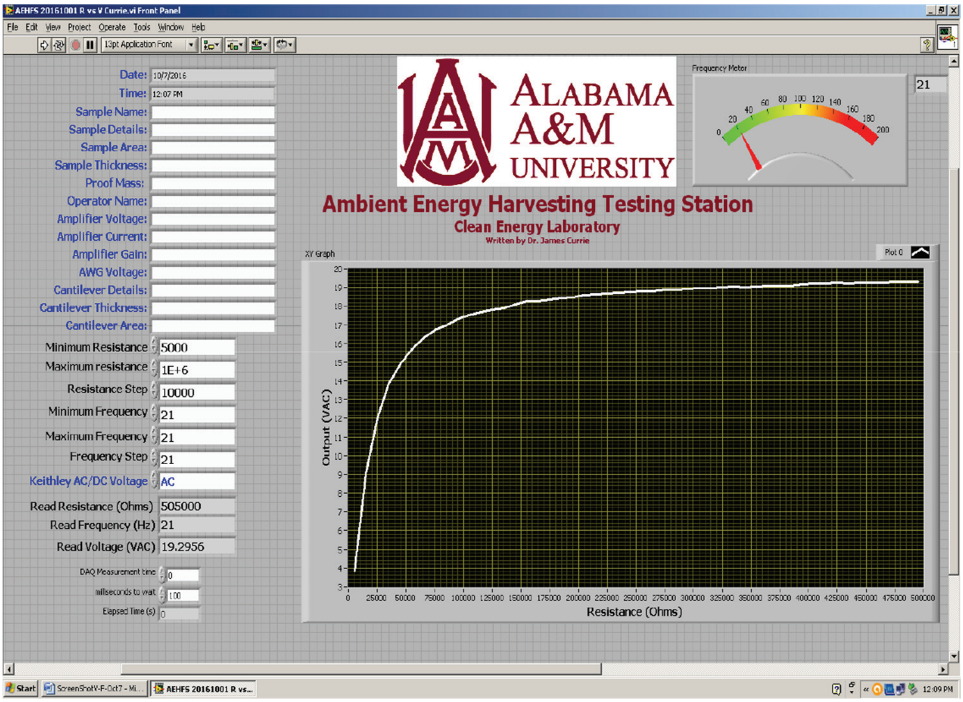

AEHFS 20161001 R vs V Currie.vi Front Panel

Date: 10/7/2016
Time: 12:07 PM
Sample Name:
Sample Details:
Sample Area:
Sample Thickness:
Proof Mass:
Operator Name:
Amplifier Voltage:
Amplifier Current:
Amplifier Gain:
AWG Voltage:
Cantilever Details:
Cantilever Thickness:
Cantilever Area:
Minimum Resistance 5000
Maximum resistance 1E+6
Resistance Step 10000
Minimum Frequency 21
Maximum Frequency 21
Frequency Step 21
Keithley AC/DC Voltage AC
Read Resistance (Ohms) 505000
Read Frequency (Hz) 21
Read Voltage (VAC) 19.2956
DAQ Measurement time 0
milliseconds to wait 100
Elapsed Time (s) 0

Ambient Energy Harvesting Testing Station
Clean Energy Laboratory
Written by Dr. James Currie

Frequency Meter 21

Figure 32 A screenshot of the control panel of the LabVIEW program.

There are some slight differences with this program, but again the first step is to enter the sample information into the control string boxes that will be recorded in the header of the data file. The next step is to select the resistances, frequencies, and other parameters for the system which will also be recorded in the data file. The starting, ending, and resistance steps are selected. Here is where the differences begin. Ensure that the starting frequency (minimum) and ending frequency (maximum) have the same value such that the system only collects data at one frequency. AC or DC voltage measurement is selected. A wait time between the measurements is selected. The next step is to run the program, which can be initiated by selecting the arrow icon or pressing <Ctrl> and <R> simultaneously. The program will ask to find the "test001.txt" file, which is located on the desktop. As the program is executed, the AWG, the PRS, and DMM are initialized. Next, a series of nested do loops are executed. In the level-1 do loop, a resistance value is sent to the PRS. The value is iterated until the maximum value is encountered, then a "false" Boolean is generated, and the do loop stops. In the level-2 do loop, a frequency value is sent to the AWG, then a "false" Boolean is generated and the do loop stops. In the level-3 do loop, voltage is measured from the DMM. Data are updated and recorded. The resistance, frequency, and voltage are written to the data file. Data are updated on the front panel. The resistance is displayed on the digital read out; the frequency is displayed on the digital read out and meter; and the voltage is displayed on the digital read out. Resistance versus voltage is plotted on an *XY* graph. The voltage measurement continues until a timeout is encountered, then a "false" Boolean is generated, the do loop stops, and the program jumps to the level-1 do loop. When a "blank" character string is encountered, the outer loop stops, the AWG output is turned off, and the PRS is programmed to 0 Ω. The program ends, and the user should locate the file "test001.txt" and rename it.

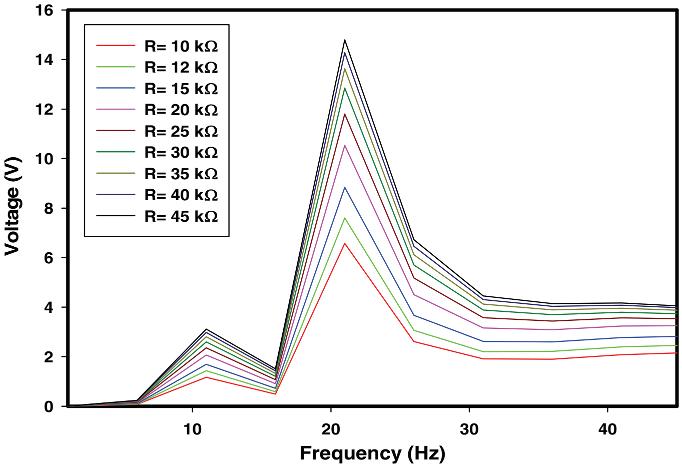

Figure 33 Output voltage vs. frequency at different values of load resistance.

6.8 Example of measurement results

From the acquired data, the following graphs were plotted for a cantilever PEH. Figure 33 shows the measured output voltages of the PEH as a function of frequency and with various electrical loads, ranging from 10 to 45 kΩ. Figure 33 shows that the maximum output voltage (occurring at resonance) increases slightly with the increase in resistive load value. Figure 34 shows the variation of the calculated power as a function of frequency, and these results agree with the available literature.

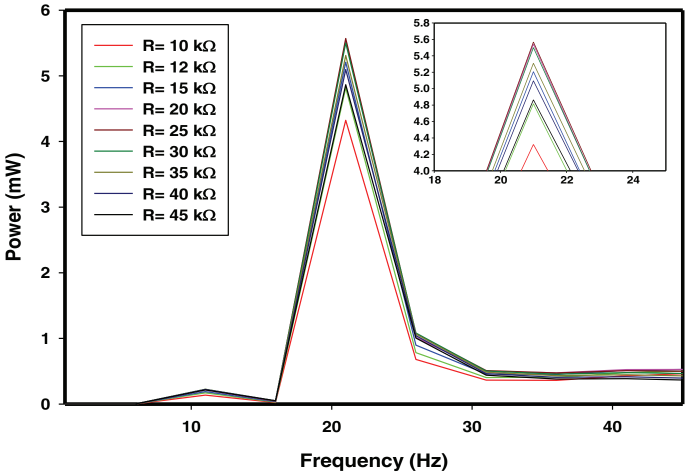

Figure 34 Output power vs. frequency at different values of load resistance, and an enlarged view around the first vibration mode.

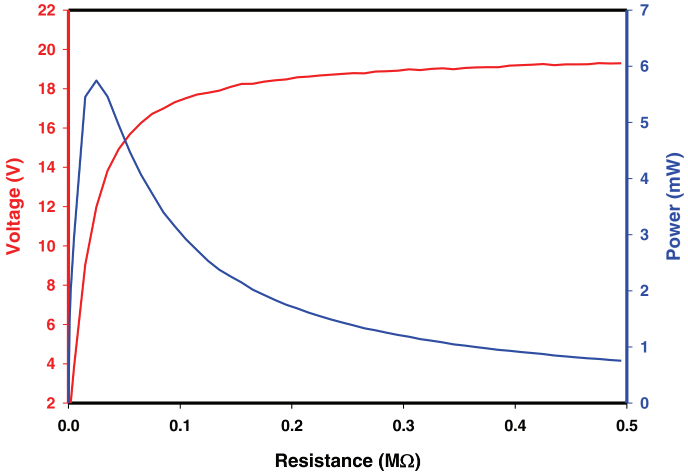

Figure 35 Output voltage and output power vs. load resistance.

Figure 35 shows the voltage measured across the load resistor and the power dissipated by it at the resonance frequency, which were extracted from Fig. 33 at the peak of the curve. A maximum output power of around 6 mW was generated into a resistive load of 0.25 MΩ at the operating frequency of 21 Hz.

Acknowledgments

The authors gratefully acknowledge financial support for this work through the National Science Foundation Grant No. RISE-HRD 1546965 and NSF (ASSURE) HBCU-UP grants. Special thanks to Dr. Chance M. Glenn and Dr. M. D. Aggarwal for their support. Technical assistance by Dr. A. A. Alomari is greatly appreciated.

References

1. A. K. Batra and A. A. Alomari, *Power Harvesting via Smart Materials*, 1st ed., SPIE Press, Bellingham, Washington (2017).
2. S. Roundy, P. K. Wright, and J. Rabaey, "A study of low-level vibrations source for wireless sensor nodes," *Comput. Commun.* **26**, 1131–1144 (2003).
3. W. G. Ali and S. W. Ibrahim, "Power analysis for piezoelectric energy harvester," *Energy Power Eng.* **4**, 496–505 (2012).
4. S. Roundy, P. K. Wright, and K. S. Pister, "Micro-electrostatic vibration-to-electricity converters," in *ASME 2002 Int. Mechanical Engineering Congress and Exposition*, pp. 487–496 (2002).
5. Y. Suzuki et al., "A MEMS electret generator with electrostatic levitation for vibration-driven energy-harvesting applications," *J. Micromech. Microeng.* **20**, 104002 (2010).
6. C. P. Le and E. Halvorsen, "MEMS electrostatic energy harvesters with end-stop effects," *J. Micromech. Microeng.* **22**, 074013 (2012).
7. P. Basset et al., "Electrostatic vibration energy harvester with combined effect of electrical nonlinearities and mechanical impact," *J. Micromech. Microeng.* **24**, 035001 (2014).
8. S. P. Beeby et al., "A micro electromagnetic generator for vibration energy harvesting," *J. Micromech. Microeng.* **17**, 1257 (2007).
9. B. Yang et al., "Electromagnetic energy harvesting from vibrations of multiple frequencies," *J. Micromech. Microeng.* **19**, 035001 (2009).
10. M. M. Wischke et al., "Electromagnetic vibration harvester with piezoelectrically tunable resonance frequency," *J. Micromech. Microeng.* **20**, 035025 (2009).
11. D. Spreemann and Y. Manoli, *Electromagnetic Vibration Energy Harvesting Devices: Architectures, Design, Modeling and Optimization*, 1st ed., Springer Science & Business Media, New York (2012).
12. T. Sato, K. Watanabe, and H. Igarashi, "Coupled analysis of electromagnetic vibration energy harvester with nonlinear oscillation," *IEEE Trans. Magn.* **50**, 313–316 (2014).
13. S. R. Anton and H. A. Sodano, "A review of power harvesting using piezoelectric materials," *Smart Mater. Struct.* **16**, 2003–2006 (2007).
14. H. S. Kim, J. H. Kim, and J. Kim, "A review of piezoelectric energy harvesting based on vibration," *Int. J. Precis. Eng. Manuf.* **12**, 1129–1141 (2011).
15. S. Saadon and O. Sidek, "A review of vibration-based MEMS piezoelectric energy harvesters," *Energy Convers. Manage.* **52**, 500–504 (2011).

16. A. K. Batra et al., “Piezoelectric power harvesting devices: an overview,” *Adv. Sci. Eng. Med.* **8**, 1–12 (2016).
17. M. E. Staley and A. B. Flatau, “Characterization of energy harvesting potential of Terfenol-D and Galfenol,” *Proc. SPIE* **5764**, 630–640 (2005).
18. L. Wang and F. G. Yuan, “Vibration energy harvesting by magnetostrictive material,” *Smart Mater. Struct.* **17**, 045009 (2008).
19. X. Dai et al., “Energy harvesting from mechanical vibrations using multiple magnetostrictive/piezoelectric composite transducers,” *Sens. Actuators, A* **166**, 94–101 (2011).
20. S. Mohammadi and A. Esfandiari, “Magnetostrictive vibration energy harvesting using strain energy method,” *Energy* **81**, 519–525 (2015).
21. J. W. Xu et al., “Right-angle piezoelectric cantilever with improved energy harvesting efficiency,” *Appl. Phys. Lett.* **96**, 152904 (2010).
22. A. J. Erturk, M. Renno, and D. J. Inman, “Modeling of piezoelectric energy harvesting from an L-shaped beam-mass structure with an application to UAVs,” *J. Intell. Mater. Syst. Struct.* **20**, 529–544 (2008).
23. X. Tang and L. Zuo, “Enhanced vibration energy harvesting using dual-mass systems,” *J. Sound Vib.* **330**, 5199–5209 (2011).
24. W. Zhou, G. R. Penamalli, and L. Zuo, “An efficient vibration energy harvester with a multi-mode dynamic magnifier,” *Smart Mater. Struct.* **21**, 015014 (2011).
25. A. Aladwani et al., “Cantilevered piezoelectric energy harvester with a dynamic magnifier,” *J. Vib. Acoust.* **134**, 031004 (2012).
26. O. Aldraihem and A. Baz, “Energy harvester with a dynamic magnifier,” *J. Intell. Mater. Syst. Struct.* **22**, 521–530 (2011).
27. M. Ferrari et al., “Piezoelectric multifrequency energy converter for power harvesting in autonomous microsystems,” *Sens. Actuators, A* **142**, 329–335 (2008).
28. H. Xue, Y. Hu, and Q. M. Wang, “Broadband piezoelectric energy harvesting devices using multiple bimorphs with different operating frequencies,” *IEEE Trans. Ultrason. Ferroelectr. Freq. Control* **55**, 2104–2108 (2008).
29. A. Alomari and A. K. Batra, “Experimental and modelling study of a piezoelectric energy harvester unimorph cantilever arrays,” *Sens. Transducers* **192**, 37–45 (2015).
30. J. T. Lin, B. Lee, and B. Alphenaar, “The magnetic coupling of a piezoelectric cantilever for enhanced energy harvesting efficiency,” *Smart Mater. Struct.* **19**, 045012 (2010).
31. V. R. Challa et al., “A vibration energy harvesting device with bidirectional resonance frequency tunability,” *Smart Mater. Struct.* **17**, 015035 (2008).
32. M. Ferrari et al., “Improved energy harvesting from wideband vibrations by nonlinear piezoelectric converters,” *Sens. Actuators, A* **162**, 425–431 (2010).
33. L. Tang and Y. A. Yang, “A nonlinear piezoelectric energy harvester with magnetic oscillator,” *Appl. Phys. Lett.* **101**, 094102 (2012).
34. A. R. Foisal, C. Hong, and G. S. Chung, “Multi-frequency electromagnetic energy harvester using a magnetic spring cantilever,” *Sens. Actuators, A* **182**, 106–113 (2012).
35. G. Liu, P. Ci, and S. Dong, “Energy harvesting from ambient low-frequency magnetic field using magneto-mechano-electric composite cantilever,” *Appl. Phys. Lett.* **104**, 032908 (2014).
36. D. Tan, Y. Leng, and Y. J. Gao, “Magnetic force of piezoelectric cantilever energy harvesters with external magnetic field,” *Eur. Phys. J. Spec. Top.* **224**, 2839–2853 (2015).
37. D. Zhu et al., “Closed loop frequency tuning of a vibration-based microgenerator,” in *Proc. Power MEMS 2008*, pp. 229–232 (2008).
38. A. Erturk and D. J. Inman, *Piezoelectric Energy Harvesting*, John Wiley & Sons, New York (2011).
39. I. Kosmadakis et al., “Vibration-based energy harvesting systems characterization using automatic electronic equipment,” *Sens. Transducers* **187**, 75–81 (2015).

40. A. Alomari et al., "A multisource energy harvesting utilizing highly efficient ferroelectric PMN-PT single crystal," *J. Mater. Sci. Mater. Electron.* **27**, 10020–10030 (2016).
41. C. R. Bowen et al., "Piezoelectric and ferroelectric materials and structures for energy harvesting applications," *Energy Environ. Sci.* **7**, 25–33 (2014).
42. K. Kanda et al., "Microfabrication and application of series-connected PZT elements," *Proc. Chem.* **1**, 808–811 (2009).
43. M. Bau et al., "Sensors and energy harvesters, based on piezoelectric films," *Proc. Eng.* **25**, 737–744 (2011).
44. W. Chang et al., "Design and fabrication of a double-sided piezoelectric transducer for harvesting vibration power," *Thin Solid Films* **529**, 39–44 (2013).
45. Y. Hu and Z. Wang, "Recent progress in piezoelectric nanogenrators as a sustainable power source in self-powered systems and active sensors," *Nano Gener.* **14**, 3–14 (2015).
46. M. Rguiti et al., "Elaboration and characterization for low frequency and wideband piezoelectric generator for energy harvesting," *Opt. Mater.* **36**, 8–12 (2013).
47. C. Wei and X. Jing, "A comprehensive review on vibration energy harvesting: modeling and realization," *Renew. Sustain. Energy Rev.* **74**, 1–18 (2017).
48. J. Zhao et al., "Investigation of d15 mode PZT-51 piezoelectric energy harvester with a series connection structure," *Smart Mater. Struct.* **21**, 105006 (2012).
49. N. H. Diyana et al., "Vibration energy harvesting using single and comb-shaped piezoelectric beam structures modeling and simulation," *Eng. Proc.* **41**, 1228–1234 (2012).
50. L. Dhakar et al., "A new harvester design for high power output at low frequencies," *Sens. Actuators, A* **199**, 344–352 (2013).
51. W. Ashtari et al., "Enhanced energy harvesting using multiple piezoelectric elements: theory and experiments," *Sens. Actuators, A* **200**, 138–146 (2013).
52. C. T. Pan, Z. H. Liu, and Y. C. Chen, "Study of broad bandwidth vibration energy harvesting system with optimum thickness of PET substrate," *Curr. Appl. Phys.* **12**, 684–696 (2012).
53. J. Song et al., "Design optimization of PVDF-based piezoelectric energy harvesters," *Heliyon* **3**, e00377 (2017).
54. A. K. Batra and M. D. Aggarwal, *Pyroelectric Materials*, SPIE Press, Bellingham, Washington (2013).
55. A. K. Batra et al., "A versatile and fully instrumented test station for piezoelectric energy harvesters," *Measurement* **114**, 9–15 (2018).

Ashok K. Batra holds a master of technology and PhD from Indian Institute of Technology, Delhi. With more than 24 years of experience in the diverse areas of solid-state physics/materials and their applications, he is now a professor of physics. His research experience and interests encompass ferroelectric, pyroelectric, and piezoelectric materials and their devices; the design, fabrication, and characterization of pyroelectric, piezoelectric, photothermal, and photovoltaic devices; nonlinear optical organic crystals; organic semiconductors; crystal growth from solution and melt; microgravity material research; nanocomposites; pyroelectric IR sensors; and chemical sensors. He is currently engaged in research related to the development of ambient energy harvesting and storage devices, nanoparticle-based chemical sensors, organic force sensors, and organic photovoltaic solar cells. He has obtained various research grants as the principal or co-investigator from the US Army/SMDC, NSF, DHS, and NASA. The NASA grant was related to the International Microgravity Laboratory-1 experiment flown aboard the Space Shuttle Discovery. He is a recipient of a NASA Group Achievement award and the Alabama A&M University School of Arts and Sciences Researcher of the Year award. He has published over 200 publications, including two books, book chapters, proceedings, review articles, and NASA TMs. He is a member of SPIE, MRS, AES, and AAS.

Bir B. Bohara is a PhD candidate in the Department of Physics (material science group), Alabama A&M University, USA. His research interests include dielectrics, pyroelectric materials, piezoelectric materials, energy harvesting, and smart systems. He has publications in peer-reviewed journals. He received his MS degree in condensed matter physics from Southern University and A&M College, Baton Rouge, Louisiana, in 2016. He worked on density functional theory as a research assistant during his MS. He also completed his master's degree in solid-state physics in 2007 from Tribhuvan University, Nepal, and served as a lecturer for 5 years. He attained his bachelor of science (BSc) degree from Tribhuvan University with a triple major in physics, chemistry, and mathematics.

James R. Currie, Jr. graduated from Athens State College with a BS degree and a double major in physics and mathematics in May 1987. He graduated from AAMU with an MS degree in physics specializing in materials science in May 2004. He graduated from AAMU with a PhD in applied physics specializing in materials science. He has many publications on various kinds of sensors, namely infrared and chemical. He has been working at NASA-George C. Marshall Space Flight Center since 1989 as an electronics engineer. Currently, he is the flight sensors team leader in the sensors, imaging, and optics branch of the Avionics Development Division in the Space Systems Department. He is currently working on flight sensors for the Space Launch System core stage. He has worked on flight sensor issues for many programs and projects, which include Shuttle Transportation System, International Space Station, Constellation, Microgravity Crystal Growth Experiments, X Vehicles (X-33, X-34, and X-37), and Rocket Engine Development and Testing programs (SSME, RD-120, J-2X, RS-83, RS-84, and Cobra and Fast Track).